AGU PUBLICATIONS

JGR

Journal of Geophysical Research: Solid Earth

RESEARCH ARTICLE
10.1002/2013JB010854

Key Points:
- New method for imaging the earthquakes source dynamics
- Fundamental source parameters of an intermediate-depth Mexican earthquake
- Slow rupture, low radiation efficiency, high stress drop, and small rupture area

Supporting Information:
- Text S1
- Figure S1
- Figure S2
- Figure S3
- Figure S4
- Figure S5
- Figure S6
- Figure S7

Correspondence to:
V. M. Cruz-Atienza,
cruz@geofisica.unam.mx

Citation:
Díaz-Mojica, J., V. M. Cruz-Atienza, R. Madariaga, S. K. Singh, J. Tago, and A. Iglesias (2014), Dynamic source inversion of the *M*6.5 intermediate-depth Zumpango earthquake in central Mexico: A parallel genetic algorithm, *J. Geophys. Res. Solid Earth*, *119*, 7768–7785, doi:10.1002/2013JB010854.

Received 14 NOV 2013
Accepted 23 SEP 2014
Accepted article online 27 SEP 2014
Published online 25 OCT 2014

Dynamic source inversion of the *M*6.5 intermediate-depth Zumpango earthquake in central Mexico: A parallel genetic algorithm

John Díaz-Mojica[1,2], Víctor M. Cruz-Atienza[1], Raúl Madariaga[3], Shri K. Singh[1], Josué Tago[1,2], and Arturo Iglesias[1]

[1]Instituto de Geofísica, Universidad Nacional Autónoma de México, Mexico, [2]Institut des Sciences de la Terre, Université Joseph Fourier, Grenoble, France, [3]Laboratoire de Géologie, Ecole Normale Supérieure, Paris, France

Abstract We introduce a method for imaging the earthquake source dynamics from the inversion of ground motion records based on a parallel genetic algorithm. The source model follows an elliptical patch approach and uses the staggered-grid split-node method to simulate the earthquake dynamics. A statistical analysis is used to estimate errors in both inverted and derived source parameters. Synthetic inversion tests reveal that the average rupture speed (V_r), the rupture area, and the stress drop ($\Delta\tau$) may be determined with formal errors of ~30%, ~12%, and ~10%, respectively. In contrast, derived parameters such as the radiated energy (E_r), the radiation efficiency (η_r), and the fracture energy (G) have larger errors, around ~70%, ~40%, and ~25%, respectively. We applied the method to the M_w 6.5 intermediate-depth (62 km) normal-faulting earthquake of 11 December 2011 in Guerrero, Mexico. Inferred values of $\Delta\tau = 29.2 \pm 6.2$ MPa and $\eta_r = 0.26 \pm 0.1$ are significantly higher and lower, respectively, than those of typical subduction thrust events. Fracture energy is large so that more than 73% of the available potential energy for the dynamic process of faulting was deposited in the focal region (i.e., $G = (14.4 \pm 3.5) \times 10^{14}$J), producing a slow rupture process ($V_r/V_S = 0.47 \pm 0.09$) despite the relatively high energy radiation ($E_r = (0.54 \pm 0.31) \times 10^{15}$ J) and energy-moment ratio ($E_r/M_0 = 5.7 \times 10^{-5}$). It is interesting to point out that such a slow and inefficient rupture along with the large stress drop in a small focal region are features also observed in both the 1994 deep Bolivian earthquake and the seismicity of the intermediate-depth Bucaramanga nest.

1. Introduction

Fracture mechanics has been the fundamental tool used by seismologists to explain seismic radiation and the propagation of seismic ruptures [*Kostrov*, 1966; *Andrews*, 1976; *Madariaga*, 1976; *Das and Aki*, 1977; *Mikumo and Miyatake*, 1978]. Dynamic source models based on mechanical considerations have thus become a powerful mean to understand fundamental aspects of the physics behind the spontaneous rupture of geological faults [*Ida*, 1972; *Palmer and Rice*, 1973; *Burridge et al*., 1979; *Day*, 1982; *Madariaga et al*., 1998; *Freund*, 1989]. These models have primarily been used to characterize the overall properties of the rupture process from a fracture mechanics point of view by integrating different friction and rheological behaviors into the source models.

Different studies have tried to estimate fault frictional parameters from well-recorded earthquakes based on kinematic source inversions of strong motion seismograms [e.g., *Ide and Takeo*, 1997; *Mikumo et al*., 2003]. Unfortunately, due to the limited bandwidth of the recorded data, these parameters were poorly resolved. Dynamic models based on such indirectly inferred parameters may thus be biased and not able to resolve the small-scale rupture dynamics [*Guatteri and Spudich*, 2000; *Spudich and Guatteri*, 2004]. Direct observation of the stress breakdown slip from near-field data, for instance, is seldom possible [*Cruz-Atienza et al*., 2009], except in some special cases where rupture propagates at supershear speeds [*Cruz-Atienza and Olsen*, 2010]. Despite this limitation inherent to the radiated wavefield from earthquake sources, the macroscopic properties (i.e., low frequencies) of seismic radiation far from the source are linked to the mesoscopic source features through the elastodynamic and fault constitutive equations governing the rupture. This constrains the space of solution models to those physically acceptable and is the reason why the dynamic source inversion of ground motions represents a more attractive alternative for imaging the source process than purely and simple phenomenological approaches based on kinematic source descriptions.

Despite the advances in computational methods, solving the earthquake elastodynamic problem in 3-D still represents an important numerical challenge for supercomputer platforms when thousands of problem solutions are required. Finite difference (FD) dynamic rupture models have provided a key strategy to overcome this problem, thanks to their numerical efficiency [e.g., *Madariaga*, 1976; *Andrews*, 1976; *Virieux and Madariaga*, 1982; *Day*, 1982; *Madariaga et al*., 1998; *Mikumo and Miyatake*, 1993; *Cruz-Atienza and Virieux*, 2004; *Cruz-Atienza et al*., 2007; *Dalguer and Day*, 2007]. In spite of this quality inherent to the FD approach, hybrid methods to propagate the wavefield from the source to the receivers at regional scales are still necessary to afford thousands of model solutions, although new and promising computational developments [*Tago et al*., 2012] may shortly allow the dynamic source imaging by means of a single and versatile numerical model.

Peyrat and Olsen [2004] attempted dynamic rupture inversion for imaging the M_w6.6 Tottori earthquake, in Japan, by means of a heuristic optimization method (i.e., neighborhood algorithm) directly from ground motion records. Subsequently, similar strategies have been used to achieve the dynamic source inversion of different earthquakes [*Corish et al*., 2007; *Di Carli et al*., 2010; *Peyrat and Favreau*, 2010; *Ruiz and Madariaga*, 2011, 2013]. In this study we introduce a novel approach for imaging earthquake source dynamics from ground motion records based on a simple source description and a parallel genetic algorithm. It follows the elliptical dynamic-rupture-patch approach introduced by *Di Carli et al*. [2010] and has been carefully verified through numerous synthetic inversion tests [*Díaz-Mojica*, 2012]. In this work we first introduce and validate the inversion method and then apply it to image the source dynamics of the M_w 6.5 intermediate-depth (i.e., intraslab) normal-faulting Zumpango earthquake, Guerrero, Mexico, ~185 km to the southwest of Mexico City. Estimates of stress drop, rupture velocity, and radiated energy (among others parameters) are obtained and discussed under the light of different and independent estimates for Mexican and worldwide earthquakes.

2. Dynamic Source Inversion Method

2.1. Source Model Parameterization

Earthquakes are highly nonlinear phenomena produced by sliding instabilities on geological faults. The stability of faults primarily depends on the initial state of stress, the medium properties, and the friction law, which is the constitutive relationship dictating the mechanical behavior of the sliding surface. For the sake of simplicity and to minimize the number of model parameters, our source model consists of a single elliptical patch in which the governing parameters are constant. This approach was first proposed by *Vallée and Bouchon* [2004] for the kinematic source inversion and then extended to the dynamic source analysis by *Di Carli et al*. [2010] and *Ruiz and Madariaga* [2011, 2013]. Following the latter works, we assume a linear slip-weakening friction law [*Ida*, 1972], which is controlled by three constitutive parameters: the static (μ_s) and the dynamic (μ_d) friction coefficients and the slip-weakening distance (D_c). Actually, for earthquake dynamics, only the difference $\mu_s - \mu_d$ matters. It is possible to use other friction laws in the inversion, such as rate- and state-dependent models, but those laws would require increasing the numerical effort for solving the direct problem. Besides, it is well known that at high slip rates, rate and state behaves like slip weakening, as shown by *Bizzarri and Cocco* [2003].

In our dynamic inversion method, the source geometry is controlled by five parameters defining the shape and orientation of an elliptical patch. These are the lengths of the two semiaxes of the ellipse, the two Cartesian coordinates of its center on the fault plane with respect to the hypocenter, and the angle of the semimajor axis with respect to the fault strike. Four more parameters complete our source model parameterization: the initial shear stress in both the elliptical patch, τ_0, and the nucleation patch, τ_0^n, which is circular and has a radius of 1.5 km, the slip-weakening distance, D_c, and the change in the friction coefficient $\Delta\mu = \mu_s - \mu_d$. We thus invert for nine parameters: five determining the geometry of the rupture patch and the other four dealing with the friction law and the initial state of stress on the fault plane (see Table 2).

Although we cannot infer the absolute prestress values on the fault, to set a reasonable reference level, we took the fault normal stress (σ_N) equal to the lithostatic load at 60 km depth (i.e., 1564 MPa) and $\mu_d = 0.5$ so that the residual fault strength is given by the Coulomb law as $\tau_d = \mu_d \times \sigma_N$ =782 MPa. This choice has no consequences in the spontaneous rupture process but provides more realistic estimates of $\Delta\mu$. To initiate rupture, the static fault strength inside the nucleation patch, τ_s^n, is set slightly below τ_0^n (i.e., $\tau_s^n = \tau_0^n - 1.5$ MPa)

so that rupture initiates with an instantaneous stress drop equal to $\tau_0^n - \tau_s^n$. Outside the nucleation zone but inside the elliptical patch, the static strength is model dependent and given by $\tau_s = \mu_s \times \sigma_N$. Rupture cannot propagate beyond the elliptical patch because μ_s is set to a very large value outside the patch as in the barrier model of *Das and Aki* [1977]. It is also possible to invert for an asperity model, as shown by *Di Carli et al*. [2010].

2.2. Forward Problem

To compute the synthetic seismograms at the stations for each dynamic source model tested during the inversion, we follow a two-step hybrid procedure. Since 3-D dynamic source modeling demands large computational time, in the first step we solve the dynamic rupture problem for a given set of source parameters within a small box by means of an efficient and very accurate finite difference approach, namely, the staggered-grid split-node (SGSN) method [*Dalguer and Day*, 2007]. Aware of the SGSN numerical properties, we have chosen a spatial grid step of 300 m with a time increment of 0.016 s all along this work in order to obtain a good compromise between the efficiency, the accuracy, and the stability of the scheme [*Dalguer and Day*, 2007]. The dynamic source problem is thus solved in an elastic cube with seismic properties corresponding to the source depth. The cube has 40 km length per edge (i.e., 134 nodes per dimension) and perfectly matched layer (PML) absorbing boundary conditions in every external face of the simulation domain [*Marcinkovich and Olsen*, 2003; *Olsen et al*., 2009]. The fault plane where the inversion scheme searches for the best rupture patch geometry is centered in the cubic domain and has 30 km length on each side.

The second step to compute the synthetic seismograms consists in propagating the wavefield from the dynamic source up to the stations. To this purpose, we use a representation theorem [*Das and Kostrov*, 1990] that combines the modulus of the slip rate history in every subfault with the corresponding point dislocation Green tensor for each station and for a given fault mechanism. The slip rate functions are the output of the dynamic source simulation, while the Green tensors for the given mechanism are computed in a layered medium with the discrete wave number (DWN) method [*Bouchon*, 1981; *Coutant*, 1989] and stored prior to the inversion. This strategy makes wavefield propagation at regional scales extremely fast when computing synthetic seismograms during forward modeling. To optimize even more the forward problem, we use average slip rate functions over fault cells containing 5 by 5 grid points (i.e., 1.5 by 1.5 km) of the finite difference mesh [*Di Carli et al*., 2010]. Verification tests of the algorithm for many different fault mechanisms and sizes have been done comparing synthetic seismograms at the free surface with those computed with independent methods, namely, the DWN method for point sources and the SGSN method for extended sources, finding excellent results [*Díaz-Mojica*, 2012].

2.3. Parallel Genetic Algorithm

For solving the dynamic source inverse problem given a set of seismological observations (i.e., ground motion records of a given earthquake), we have developed a heuristic optimization method based on genetic algorithms (GA) [*Holland*, 1975; *Goldberg*, 1989]. Since the solution of the inverse problem requires solving thousands of computationally expensive forward problems, like the dynamic rupture modeling concerned in this study, parallel optimization strategies are the only way to solve the inverse problem. Our method takes advantage of the GA strategy to incorporate the Message Passing Interface (MPI) for simultaneously solving a large number of forward problems in parallel. In GA a randomly generated initial model population evolves following three basic mechanisms of natural evolution: selection, crossover, and mutation. Similar to other parallel optimizing methods [e.g., *Pikaia*, 2002; *Fernández de Vega and Cantú-Paz*, 2010], to equitably distribute the workload in the computing platform, the same number of models is assigned to each computing core so that the size of the model population is always a multiple of the number of processes required for the parallel inversion procedure. This guarantees that each core solves the same amount of forward problems per generation (i.e., per algorithm iteration, Figure 1). Once the forward problem is solved for the whole population, the output synthetic seismograms are gathered in the master processor to pursue with the next GA steps (i.e., selection, crossover, and mutation; see Figure 1).

Selection is one of the key mechanisms promoting the evolution of a population. Different selection criteria have been proposed for GA in the literature [e.g., *Goldberg*, 1989; *Iglesias et al*., 2001; *Cruz-Atienza et al*., 2010]. In all cases, selection is based on the aptitude of the individuals to survive over generations given some kind of "environmental" conditions. In our method, each individual of the population corresponds to a set of source model parameters. The aptitude of an individual is given by a misfit function between the associated synthetic seismograms, d_s, produced by the forward problem solution, and the observed

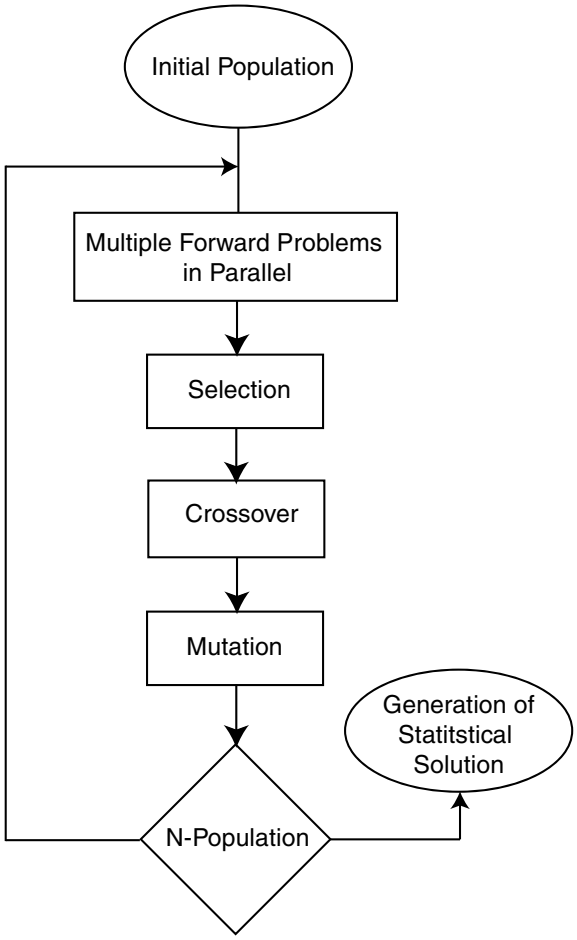

Figure 1. Flow diagram of the parallel genetic algorithm developed in this study.

seismograms, d_o (i.e., data). The misfit function we have used is based on the correlation function between the signals, and it is composed by two main terms (equation (1)). The first term is known as the semblance, which provides a measure of the waveforms similarity [*Spudich and Miller*, 1990; *Cruz-Atienza et al.*, 2010]. The second term involves the time shift of the maximum cross-correlation coefficient between both signals so that it provides a control of their phases (absolute arrival times).

$$M = 0.5\left[1 - \frac{\text{cross}(d_s,\ d_o)}{\text{auto}(d_s) + \text{auto}(d_o)} + \frac{|\delta\tau| - \tau_c}{2\tau_c}\right] \quad (1)$$

In equation (1), auto(d_s) and auto(d_o) are the autocorrelation of the synthetic and observed data, respectively, and cross($d_s - d_o$) is the cross correlation of both signals. In the last term, $|\delta\tau|$ is the time shift absolute value for the maximum cross-correlation coefficient and τ_c is a reference delay, approximately given by half the source duration. We found $\tau_c = 2$ *s* to be a good value for this earthquake, properly weighting both misfit terms. The misfit function becomes zero if both signals are the same. Adding the phase term was critical to resolve rupture causality in our dynamic source model, because time delays in the spontaneous rupture propagation (which are translated into delays of radiated waves) are directly related to the prestress and friction parameters over the fault.

Each iteration of the GA algorithm starts by estimating the aptitude for all individuals through equation (1). To select the fittest models based on their aptitude, we use the biased roulette criterion [*Goldberg*, 1989], which attributes a survival probability to each model depending on the associated misfit function value. Those with the higher aptitude (i.e., lower values of *M*) have the larger probabilities of survival. To preserve the best individuals in the next generation, we guarantee the survival of an elite corresponding to the 15% top models. After selection, the population size remains the same.

The values of the model parameters per individual are binary coded to form a string of bits (i.e., chromosome), which represents the genetic footprint of the associated source model. To evolve, the population exchanges information via the crossover of genes (i.e., bits) between pairs of individuals (Figure 1). For this purpose, we have tested different strategies and found that coupling the best half of the population with the other half systematically yields robust and monotonic convergence of the problem solution. Cutting both chromosomes in a randomly selected gen and exchanging the second half of each chromosome does the crossover between a pair of models. After the crossover, an evolving percentage of the population is mutated to promote diversity (Figure 1). This percentage evolves linearly from high to low values in the inversion (i.e., from 60% to 10%), allowing a large exploration of the model space at the beginning and the exploitation of the best solution neighborhoods by the end of the inversion. Mutation is simply performed by changing the value of a randomly selected gene (bit) in the chromosome of a randomly selected individual.

The parallel GA method has been optimized in several ways. Models that have been computed in any previous generation are not computed again. In these cases, the algorithm attributes the misfit value previously obtained to repeated models. Besides this, after 1.5 s of each dynamic rupture FD simulation, the program looks at the slip rate over the whole fault to determine whether the rupture is propagating (i.e., it

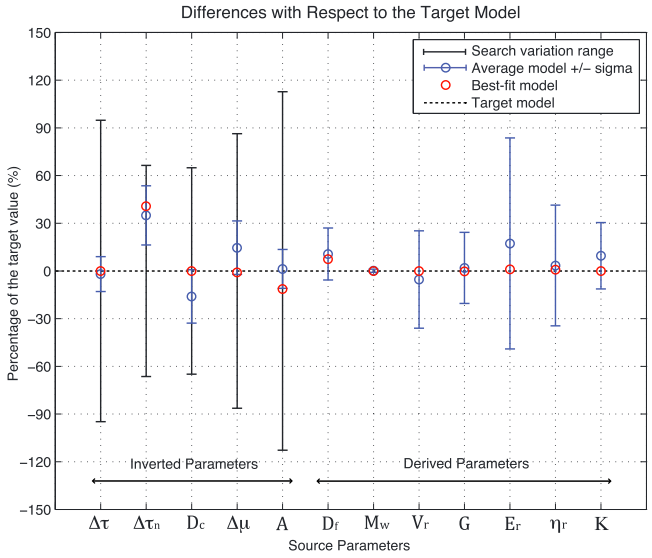

Figure 2. Source parameters convergence, uncertainty estimates, and search variation ranges in the synthetic inversion. The variation range for the rupture area, A, has been divided by 5 for plotting purposes.

verifies if the slip rate is different from zero somewhere). If not, it automatically stops the FD computation, attributes a misfit value of 0.5 to the model, and continues solving the next forward problem.

2.4. Multiscale Inversion and Error Estimates

We follow a GA multiscale inversion approach consisting of two successive steps: an initial coarse inversion (i.e., with low sampling rate) exploring the full model space and a second and finer inversion (i.e., with high sampling rate) exploring the surroundings of the best solution found in the first inversion. The parameter ranges of the finer grid inversion were chosen so that values of the best solution from the coarse inversion lie in the middle of the ranges. Several synthetic inversion tests were carried out by *Díaz-Mojica* [2012], considering the problem setup discussed later in section 3 for the 2011 Zumpango intraslab normal-faulting event studied here (Figure 3). One representative test was selected and discussed in the supporting information of this paper. Results from the test are excellent as shown in Figure 2, where we summarize the outcomes of such synthetic inversion in terms of differences between the best fit model parameters (red circles) and those of the target model. Note that the source geometrical parameters are lumped, for displaying purposes only, into the rupture area, A, that depends on the length of both semiaxis of the elliptical patch. Recovery of the entire rupture geometry may be appreciated in Figure S1. Since the dynamic fault strength is fixed and equal to $\tau_d = 782$ MPa (see section 2.1), stress estimates may be expressed in terms of the dynamic stress drops, $\Delta\tau_n$ and $\Delta\tau$, inside and outside the nucleation patch, respectively. Beside the inverted parameters (left double arrow in Figure 2), we also report results for some derived parameters (right double arrow) introduced later in section 3.3, such as the rupture speed (V_r) and both the fracture (G) and radiated (E_r) energies, among others. Except for the stress drop inside the nucleation patch ($\Delta\tau_n$), which differs from the target value by about 40%, the other eleven source parameters differ by less than ~5% of the target value. Moreover, the second GA sampling gives information about the probability density function (PDF) of the model parameters (Figure S4). Details of the PDF generation from our GA are given in the supporting information. Although the velocity structure and both the source location and mechanism were known in this test, considering the high nonlinearity of the problem and the large model space explored in the inversion (i.e., between 60% and more than 90% of the actual parameter values, black vertical lines in Figure 2 and Table 2), this test provides confidence in our source model parameterization and the GA multiscale approach for imaging the earthquakes source dynamics.

However, given the nonlinearity of the problem and the uncertainties in the source model, the velocity structure, and the source location and mechanism, the best fit single solution model is not very meaningful for real earthquakes. We thus propose a statistical procedure to generate a set of solution models based on the sensitivity of the associated synthetic seismograms. The criterion used to select the solution models aims to guarantee that the three components of the observed seismograms lie within the standard deviation band around the average of the solution synthetics. Yet due to the strong sensitivity of ground motions to small perturbations of the dynamic source parameters, only segments of the observed seismograms are likely to fall within the band. This is true even for synthetic inversion tests (Figure S2), where the solution models are very close to the target one and both the velocity structure and the source location and mechanism are known (see the supporting information).

Following *Cruz-Atienza et al*. [2010], in order to establish a quantitative criterion for selecting the solution models, we define the area described by the observed seismograms outside the synthetics standard deviation band relative to the area of the band as follows:

$$S_R = \frac{100}{S_b}\int_0^T g(t)\mathrm{d}t, \tag{2}$$

where

$$S_b = 2\int_0^T \sigma(t)\mathrm{d}t \tag{3}$$

and

$$g(t) = \begin{cases} |d_s - d_o| - \sigma & \forall\ t \ni \sigma \le |d_s - d_o| \\ 0 & \forall\ t \ni \sigma > |d_s - d_o| \end{cases}.$$

In these equations, $\sigma(t)$ represents the standard deviation function associated with the solution models synthetics, S_b is the area of the standard deviation band around the mean, d_s and d_o are the synthetic and the observed data, respectively, T is the seismograms duration, and t is the time. To satisfy the selection criterion, S_R must be smaller than a given percentile value. This procedure makes it possible to quantify the error of the problem solution in the sense that for each model parameter, we obtain a set of values satisfying the same misfit criterion with respect to the observed data.

The way we translate the set of solution models into a single preferred (i.e., representative) model is through a weighted average involving the misfit function M (equation (1)) of every solution model. If p is a given source parameter and n is the number of solution models, then the weighted average of that parameter, $\hat{p}$, is computed as follows:

$$\hat{p} = \frac{1}{\sum_{j=1}^{n}\alpha_j}\sum_{i=1}^{n} p_i\alpha_i \tag{4}$$

where

$$\alpha_i = \mathrm{nint}\left(\frac{M_{\mathrm{worst}}}{M_i}\right)$$

and M_{worst} is the largest misfit value in the whole set of solution models. In both equations, the subscripts refer to the current model. Function nint means the nearest integer. This average makes the best models to outweigh the rest of the models without affecting the actual parameter values per model and may be applied to both source average and fault-extended quantities.

Figure 2 also shows, for the synthetic inversion test, average values using equation (4) for all parameters (blue circles) along with the associated standard deviations (blue lines) (see also Figure S4). In this case, the selection criterion was such that $S_R < 25$ % so that 325 models among the 27,000 tested models during the inversion procedure were selected to establish the final solution (see details in the supporting information). Except for the stress drop in the nucleation patch, the average solution is slightly off but within ~15% of the target model, and the standard deviation around the average contains the target value for each of these parameters (see also Figure S4).

As discussed earlier, although in this synthetic test (where no model uncertainties are present) the best fit model is closer to the target than the average solution (see Table 3), in real earthquake conditions, where uncertainties are often present, a set of solution models translated into an average solution with associated standard deviations should always be more representative of the actual problem solution provided that the model parameters have a normal distribution [*Menke*, 2012; see Figure S4 in the supporting information]. This can be seen in Table 3, where errors for the average models in different synthetic tests are significantly smaller than those of the best fit models if uncertainties are present in the event location or the velocity structure (see the supporting information for a description of the tests). Thus, if a good knowledge of these attributes is available, then several fundamental parameters like the average rupture speed (V_r), the rupture area (A) and the stress drop ($\Delta\tau$), which are very difficult to resolve in kinematic source inversions, are well constrained in our dynamic source inversion, with formal errors smaller than ~30%, ~12%, and ~10%, respectively. In contrast, derived parameters, such as the radiated energy (E_r), the radiation efficiency (η), and the fracture energy (G) have larger errors around ~70%, ~40%, and ~25%, respectively, but smaller than those resulting from

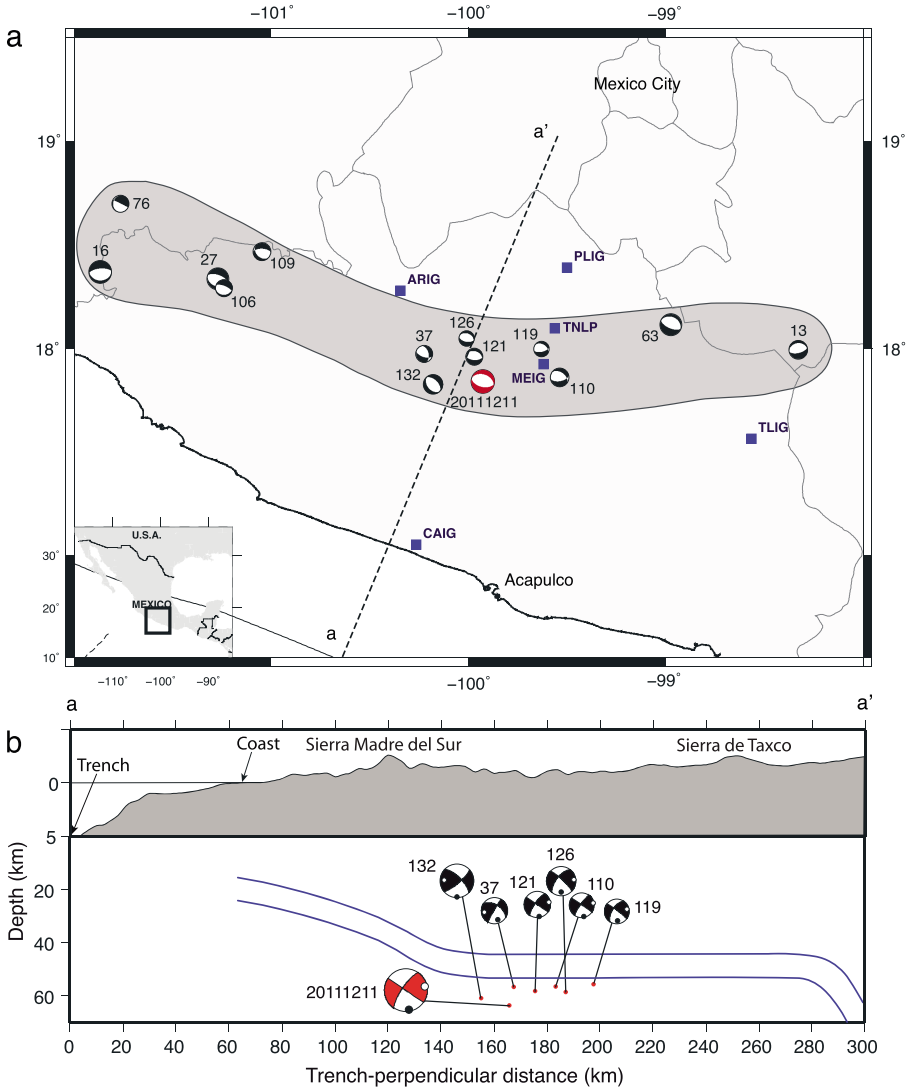

Figure 3. (a) Zumpango earthquake location and mechanism (red beach ball), stations location (blue squares), and tectonic setting. (b) Blue lines depict the subducted Cocos plate as images by *Pérez-Campos et al*. [2008]. Modified after *Pacheco and Singh* [2010].

the use of other methods [*Venkataraman and Kanamori*, 2004]. Mean values reported for the Zumpango earthquake in sections 3 (Table 3) and 4 are thus subject to these errors because of the inversion procedure, provided that the uncertainties are small in the velocity model, the earthquake location, and the mechanism.

3. The M_w 6.5 Zumpango Earthquake

The Zumpango earthquake of 11 December 2011 (1:47:28.4 GMT), in the State of Guerrero was an intraslab normal-faulting event in the subducted Cocos plate at 62 km depth, with an epicenter about 160 km from the Middle American trench (~95 km inland from the coast). It was strongly felt in Mexico City located ~185 km to the north-northeast of the epicenter, where no significant damage occurred. However, three casualties and several injuries due to landslides and the collapse of small structures were reported in Guerrero. Moment magnitude, M_w, of the earthquake reported in the Global centroid moment tensor (CMT) web page (www.globalcmt.org) is 6.5, with one of the nodal planes of the focal mechanism given by $\varphi = 284°$, $\delta = 34°$, $\lambda = -84°$. Relocation of the earthquake and centroid moment tensor (CMT) inversions using local/regional data yield the epicenter at 17.84°N and −99.93°E, with one of the nodal planes described by $\varphi = 277°$, $\delta = 44°$, $\lambda = -107°$ (red beach ball, Figure 3). This mechanism better explains the relatively low

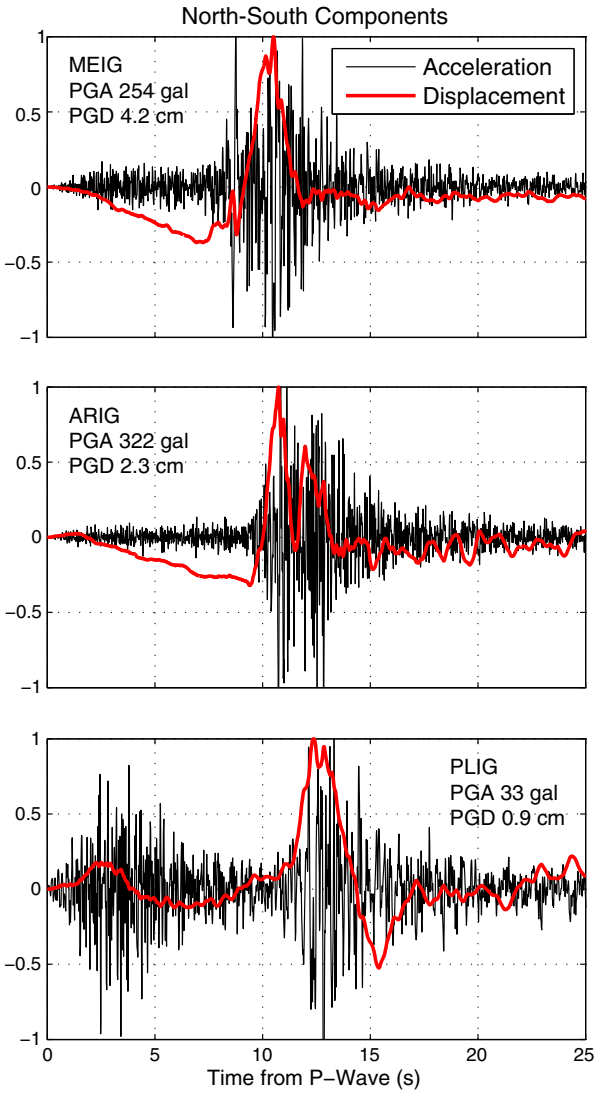

Figure 4. Observed raw data of the Zumpango earthquake at three different stations. Accelerations (solid black) and displacements (red).

S wave amplitude observed at stations CAIG and PLIG (Figure 3). Five stations (MEIG, ARIG, PLIG, CAIG, and TLIG) of the Servicio Sismológico Nacional (SSN, Instituto de Geofísica, www.ssn.unam.mx) network and one of the Instituto de Ingeniería (II) free-field strong motion network (TNLP station), with epicentral distances less than 155 km, were chosen for the analysis (Figure 3). The SSN stations are equipped with a broadband (BB) STS-2 seismometer and a Kinemetrics FBA-23 accelerometer connected to a 24 bit Quanterra digitizer, while that from the II is equipped with a Kinemetrics Altus accelerograph.

3.1. Tectonic Setting and Recorded Data

The hypocenter of the Zumpango earthquake is located inland where the ~15° dipping subducted slab unbends to become subhorizontal [*Suárez et al.*, 1990; *Singh and Pardo*, 1993; *Pérez-Campos et al.*, 2008; *Kim et al.*, 2010]. This region is characterized by normal-faulting intraslab seismicity of downdip extension type [*Pacheco and Singh*, 2010]. The intraslab seismicity of this region is located in the mantle lithosphere a few kilometers below the subducting oceanic crust. Focal mechanisms shown in Figure 3 (black and white beach balls) correspond to the events studied by *Pacheco and Singh* [2010] and form, along with the Zumpango quake, a fringe (grey shade) to the north of a ~50 km wide region which is nearly devoid of seismicity. The extensional stress regime characterizing this fringe may be explained by strain concentrations in the external part (i.e., convex and deeper part) of the slab bend [*Lemoine et al.*, 2002].

The BB seismograms of the closest stations, MEIG, ARIG, and PLIG of the SSN network were saturated. For this reason, we double integrated the acceleration records to get the displacement seismograms for the inversion. The same procedure was followed for the TNLP record. A simple integration was performed on BB velocities recorded at CAIG and TLIG. Figure 4 presents raw data of the north-south component for three of the closest stations. Although the maximum peak ground acceleration was observed at ARIG (322 gal, $\Delta = 65$ km), a maximum displacement of 4.2 cm was recorded in the closest station, MEIG ($\Delta = 34$ km). As mentioned earlier, an anomalous low-amplitude *S* wave train was observed at PLIG. This can be clearly seen in the acceleration records where both *P* and *S* waves trains at that station have similar amplitude envelopes, as compared to the other two stations. Detailed CMT inversions using local data revealed the PLIG station to be located close to *S* wave nodal plane.

The displacement seismograms (red traces) at MEIG and ARIG show a similar near-field ramp between the *P* and *S* waves. The width and shape of the *S* pulses, however, differ. Two main observations emerge: (1) the *S* train at MEIG to the east of the epicenter is narrower (by about 1.0 s) than the one observed to the northwest, at ARIG, and (2) two separated pulses are observed at ARIG but only one at MEIG. Despite the short rupture process of the earthquake (about ~3.5 s as measured from the width of the *S* waves displacement

Table 1. Layered Medium Used in This Study for the Guerrero Region [From *Campillo et al*., 1996] With Rock Quality Factors Determined From Regressions by *Brocher* [2008]

Thick (km)	V_P (km/s)	V_S (km/s)	ρ (gr/cm^3)	Q_P	Q_S
5.0	5.37	3.1	2.49	619	309
12.0	5.72	3.3	2.60	697	348
28.0	6.58	3.8	2.88	932	466
∞	8.14	4.7	3.38	1539	769

pulses), these observations reveal complexity of the source process (i.e., two main seismic radiation patches) and suggest rupture directivity toward MEIG and away from ARIG. To study the source dynamics, the displacement seismograms at the six stations were band-pass filtered (four-poles one-pass (i.e., causal) Butterworth filter) between 0.02 Hz and 0.25 Hz and then inverted with our GA method. Prior to the inversion, the observed seismograms were cut at the *P* wave arrival times and then aligned with the theoretical ones for the source location and structure considered in the study (Table 1, red curves in Figure 6). This choice is critical since a hypocenter mislocation would directly bias the source model as a consequence of wrong predictions of the *S-P* arrival times.

3.2. Dynamic Source Inversion Results

We carried out several GA inversion tests considering both nodal planes obtained from the regional CMT inversion and different velocity structures including the ultraslow layer below the continental crust reported in previous studies [*Pérez-Campos et al*., 2008; *Song et al*., 2009]. Based on the quality of waveform fits, our results indicate that the more plausible fault plane is the one dipping to the north-northeast, reported in section 3 ($\varphi = 277°$, $\delta = 44°$, $\lambda = -107°$), and that the simple one-dimensional velocity structure for the Guerrero region (Table 1), reported by *Campillo et al*. [1996], with rock quality factors obtained from regressions by *Brocher* [2008], provides the best overall result.

Five hundred four individuals formed the model population in the final two-step multiscale inversion, consisting of 50 generations per step. This makes a total of 50,400 dynamic source models tested during the whole inversion procedure. Using 168 processors of our cluster Pohualli, the multiscale inversion lasted about 24 h. Table 2 presents both the model space and the parameters sampling rates considered in each one of the two successive inversions steps. The numerical parameters used for the forward problem are given in section 2.2 and those setting the GA algorithm in section 2.3.

Figure 5 presents the evolution of the misfit function, *M* (equation (1)), for the whole inversion procedure. The multiscale approach has successfully converged. After the first 50 generations searching for solutions in a large and coarsely sampled model space, the second and finer inversion significantly improved the solution of the problem by reducing 42% the misfit of the population median and 22% the best fitting model misfit. However, during the entire inversion process, the population lying between the 25 and 75 percentiles (blue bars) remained

Table 2. Synthetic Inversion Model Space, as Defined by the Lower and Upper Variation Limits, and the Corresponding Increments Per Parameter[a]

	Coarse Inversion			Fine Inversion		
Parameter	Lower	Upper	Increment	Lower	Upper	Increment
Semiaxis 1 (km)	4.0	14.0	0.2	2.8	6.8	0.05
Semiaxis 2 (km)	4.0	14.0	0.2	4.2	8.2	0.05
Along strike (km)	−5.0	5.0	0.2	−3.0	3.0	0.05
Along dip (km)	−5.0	5.0	0.2	1.8	5.8	0.05
Angle (deg)	0.0	90.0	5.0	40.0	90.0	2.0
τ_0 (MPa)	800.0	860.0	0.2	830.0	860.0	0.005
τ_0^n (MPa)	800.0	860.0	0.2	800.0	830.0	0.005
$\Delta\mu$	0.018	0.056	0.0002	0.018	0.038	0.00005
D_c (m)	0.3	1.4	0.02	0.5	0.9	0.002

[a]The first five parameters define the geometry of the elliptical patch, while the other four describe the prestress conditions and the friction law (see text). The fault normal stress, σ_N, and the dynamic friction coefficient, μ_d, are constant and equal to 1564 MPa and 0.5, respectively (see section 2.1). As a reference, the best model yielded by the coarse inversion has the following parameters: 4.8 km, 6.2 km, −0.2 km, 3.8 km, 65°, 845.4 MPa, 804.4 MPa, 0.0282, and 0.7 m, respectively.

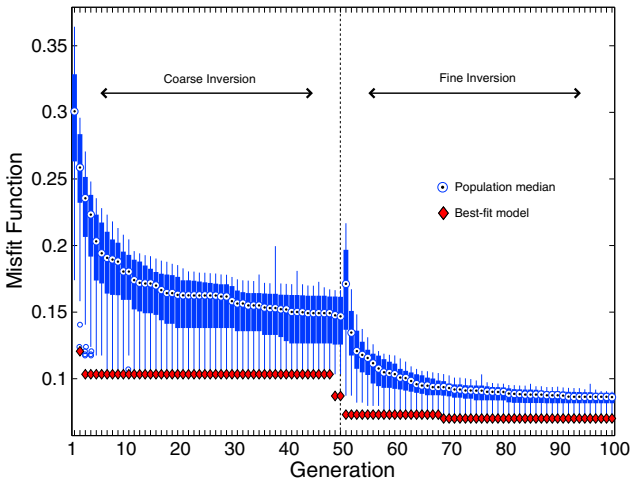

Figure 5. Misfit function evolution for the multiscale GA inversion of the Zumpango ground motion records.

significantly sparser around the median than for the synthetic inversion case (compare with Figure S3). This was expected considering the simplicity of the source model we have adopted for inverting real data.

A comparison of the observed seismograms (red curves) with those produced by the inversion is shown in Figure 6. By taking a selection criterion such that $S_R = 100\%$ (equation (2)), our final set of solution models consists of 300 individuals. The average seismograms (black curves) from this sample along with the corresponding standard deviation envelopes (black dotted curves) are also plotted in the figure, with the synthetic waveforms associated to the best model solution shown in blue. The overall fit at the six stations is excellent, although there are minor problems with the arrival times and amplitudes of the *S* wave at some stations. After many inversions, we concluded that these problems are not due to an error in the focal mechanism but to errors in the velocity structure and/or source location.

Our set of solution models is projected into the fault plane as a single source model through a weighted average defined in equation (4). The resulting quantities are shown in Figure 7b, where the average source

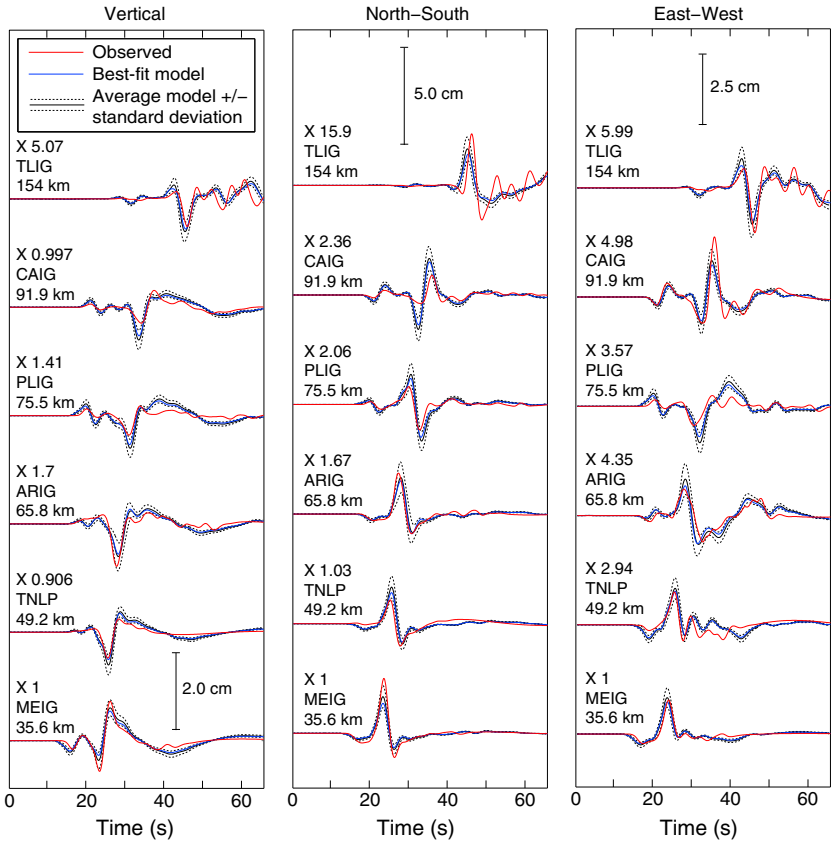

Figure 6. Zumpango earthquake seismograms fit produced by the GA inversion procedure. Seismograms are band-pass filtered between 0.02 Hz and 0.25 Hz with a one-pass (causal) Butterworth filter.

model (ASM) solution is plotted in terms of the final slip, the peak slip rate, the local rupture speed normalized by 4.7 km/s (i.e., the *S* wave velocity in the source region), the stress drop, the change in the friction coefficient, and the slip-weakening distance (Table 1). For comparison, the best fit model (BFM) is also shown in Figure 7a. As discussed earlier (section 2.4), because of the uncertainties in the propagation medium, source location, and focal mechanism, we expect the ASM to be more representative of the earthquake's actual source than the BFM. Unmodeled effects related to these factors will more easily bias the BFM. Despite this, both models share important features, such as the direction of rupture propagation, the locations of the slip rate maxima, and the overall rupture speed variability. The values of the inverted parameters are given in Table 4. It is interesting to see that both solutions indicate updip rupture propagation. On the other hand, theoretical predictions for the *S* wave pulse widths at stations ARIG and MEIG reveal that the widths may be satisfactorily explained by both updip and downdip rupture propagation (not shown). For this reason, we performed a complementary test forcing rupture propagation in the downdip direction. We find that (1) the misfit function for the best solution model was about 3 times larger than the corresponding value for updip solutions (Figure 7) and that (2) the overall dynamic source parameters reported in Table 4 are essentially the same regardless of the rupture direction. Thus, the uncertainty in the rupture directivity has little effect on our estimated dynamic source parameters.

3.3. Estimation of Dynamic Source Parameters

Based on our dynamic inversions, several interesting estimates of the source process may be obtained. Let Σ be the fault surface with unit normal vector $\boldsymbol{\nu}$. By neglecting the energy required for creating a new unit fault surface, $\iint 2\gamma_{\text{eff}}\, d\Sigma$, which is a reasonable proxy along preexistent faults, the balance of energy partition during rupture leads us to define the radiated energy as [*Rivera and Kanamori*, 2005]

$$E_r = \frac{1}{2}\iint D_f(\boldsymbol{\tau}_0 + \boldsymbol{\tau}_1)\boldsymbol{\nu} d\Sigma - \iint d\Sigma \int_{t_0}^{t_1} \boldsymbol{\tau}(t)\dot{D}(t)\boldsymbol{\nu} dt, \tag{5}$$

where $\boldsymbol{\tau}_0$ and $\boldsymbol{\tau}_1$ are the initial and final values of the stress tensor, $\boldsymbol{\tau}(t)$, respectively, $\dot{D}(t)$ is the slip rate function, D_f is the final slip, and $t_1 - t_0$ is the rise time in every point of Σ. It turns out that the initial state of stress, $\boldsymbol{\tau}_0$, which is present in both terms of the right-hand side (implicit in the second term), cancels out [*Kostrov*, 1974; *Rivera and Kanamori*, 2005] so that equation (5), expressed in terms of fault tractions, $\tau(t) = \boldsymbol{\tau}(t)\boldsymbol{\nu}$, and carrying out the surface integrals, may be rewritten as

$$E_r = A\left\{\frac{1}{2}(\tau_0 - \tau_d)D_f - \int_{t_0}^{t_1}[\tau(t) - \tau_d]\dot{D}(t) dt\right\}, \tag{6}$$

where A is the rupture area, $\tau_d = \boldsymbol{\tau}_1\boldsymbol{\nu} = \mu_d\,\sigma_N$ is the final fault traction, and both terms in the brackets now represent cumulative quantities over Σ. Since $\tau(t) - \tau_d = 0\ \forall\ t \geq t_c$ for our slip-weakening friction law, where t_c is the stress breakdown time required for the slip, D, to reach the critical value D_c and $dD = \dot{D}(t)dt$, equation (6) may be approximated as

$$E_r = A\left\{\frac{1}{2}(\tau_0 - \tau_d)D_f - \int_0^{D_c}[\tau(D) - \tau_d] dD\right\}, \tag{7}$$

where the first term, ΔW_0, represents the available potential energy for the dynamic process of faulting [*Kanamori and Brodsky*, 2004] and the second one,

$$G_c = \int_0^{D_c}[\tau(D) - \tau_d] dD, \tag{8}$$

is called the specific (i.e., per unit area) fracture energy [*Kostrov*, 1974] and represents the mechanical work done by fault tractions in a point during the stress breakdown. Cumulative values of this quantity over Σ lead to the definition of the total fracture energy $G = A \cdot G_c$.

One property of equation (7) is that, as expected, the radiated energy does not depend on the absolute stress levels at the source. Instead, E_r may be directly estimated from the static ($\Delta\tau = \tau_0 - \tau_d$) and dynamic ($\tau(D) - \tau_d$) stress drops. Furthermore, all quantities involved in the equation are known from the dynamic source models produced by the inversion. We can thus estimate the radiation efficiency [*Husseini*, 1977]

$$\eta_r = \frac{E_r}{\Delta W_0} = \frac{E_r}{E_r + G}, \tag{9}$$

which, in terms of the seismic moment, M_0, the shear modulus, μ, and $\Delta\tau$, may be approximated (i.e., by assuming $\tau_s = \mu_s\sigma_N = \tau_0$) as $\eta_r = (2\mu/\Delta\tau)(E_r/M_0)$ [*Kanamori and Brodsky*, 2004]. This is an important parameter

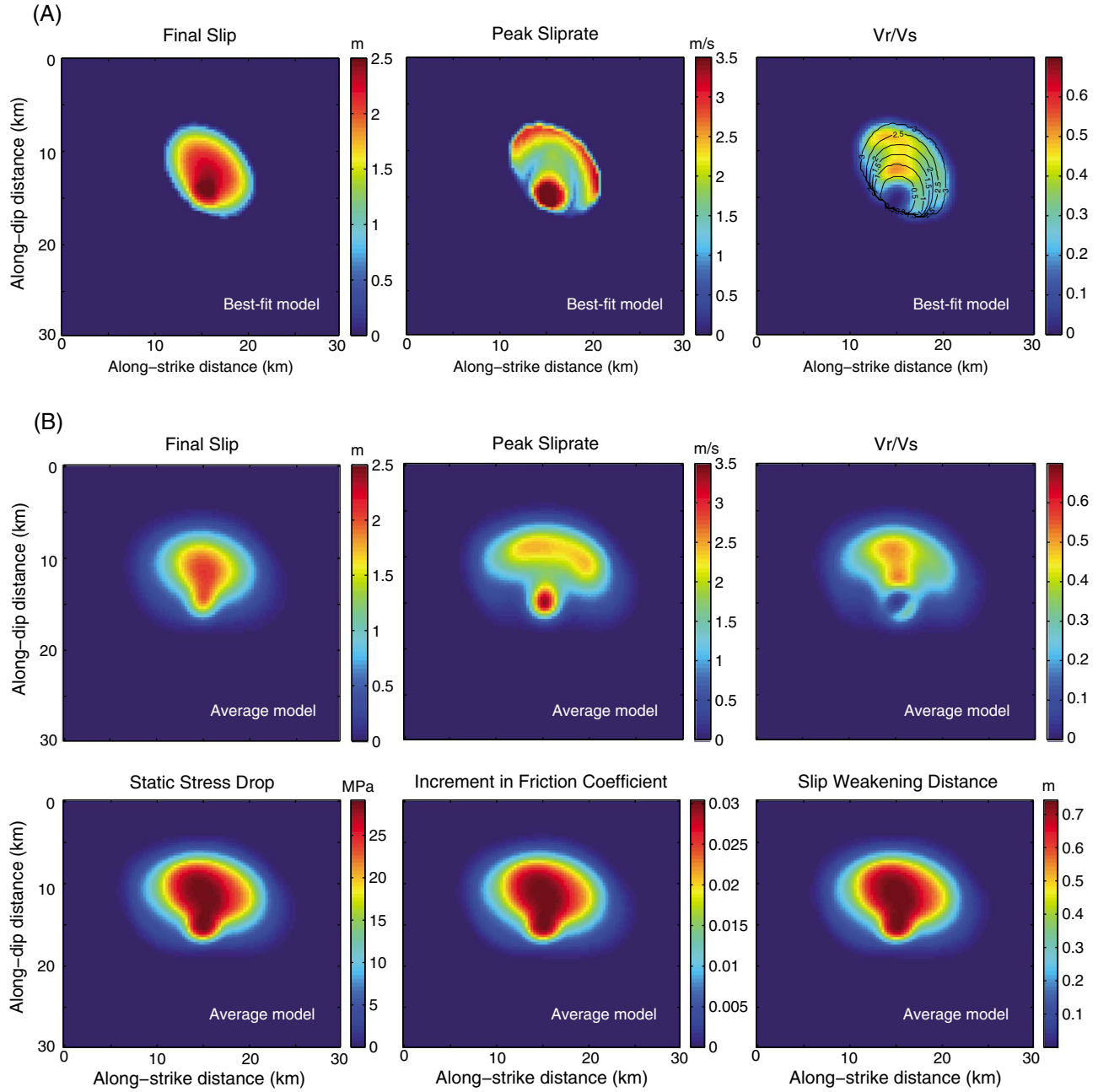

Figure 7. Fault solutions for (a) the best fit and (b) the average models of the Zumpango earthquake. Best fit model solutions for the stress drop ($\Delta\tau$), the increment of friction coefficient ($\Delta\mu$), and the slip-weakening distance (D_c) are those reported in Table 4 over the same ellipse shown in Figure 7a.

expressing the amount of energy radiated from the source as compared to the available energy for the rupture to propagate. For some earthquakes, it has been determined directly from seismological observations [e.g., *Singh et al.*, 2004; *Venkataraman and Kanamori*, 2004].

Another parameter revealing the dynamic character or criticality of earthquakes is the nondimensional parameter kappa, *K*, introduced by *Madariaga and Olsen* [2000], that may be expressed in terms of $S = (\tau_s - \tau_0)/\Delta\tau$ [*Andrews*, 1976] as

$$K = \frac{\Delta\tau}{\mu(S+1)} \cdot \frac{L}{D_c}, \tag{10}$$

Table 3. Model Errors for Different Synthetic Inversion Tests[a]

Inversion Test Description	Best Fit Model Error	Average Model Error
No model uncertainty	5.2 ± 11.8 (%)	10.1 ± 10.2 (%)
8 km epicentral mislocation	47.6 ± 39.8 (%)	31.5 ± 34.1 (%)
5% velocity structure uncertainty	15.1 ± 11.3 (%)	15.5 ± 11.9 (%)
Zumpango up to 0.5 Hz seismograms[b]	31.6 ± 20.7 (%)	20.1 ± 15.4 (%)

[a]A description of each test is found in the supporting information. Each model error corresponds to the average and standard deviation of the percentile differences with respect to the target model parameters.
[b]This test corresponds to the inversion of the Zumpango earthquake real seismograms band-pass filtered between 0.02 Hz and 0.5 Hz (see Figure S7). Errors are computed with respect to the average values reported in Table 4, which were obtained from the same seismograms but band-pass filtered between 0.02 Hz and 0.25 Hz.

where L represents a source characteristic length that, following *Ruiz and Madariaga* [2011], we took as the smaller semiaxis of the elliptical patch. Kappa has also been used in the literature to characterize the rupture process of several earthquakes [e.g., *Madariaga and Olsen*, 2000; *Di Carli et al*., 2010; *Ruiz and Madariaga*, 2011] and reveals the dynamic condition of a fault to steadily break with a given rupture speed.

Table 4 reports the derived dynamic source parameters for the Zumpango earthquake using either equations (7) to (10) or the solution models kinematics averaged over the rupture surface. These include the seismic moment, M_0, the stress drop, $\Delta\tau$, the radiated seismic energy, E_r, the fracture energy, G, the radiation efficiency, η_r, the rupture velocity, V_r, and the final slip, D_f.

E_r obtained here from dynamic source inversion is $(5.4 \pm 3.1) \times 10^{14}$ J for the average solution and 3.1×10^{14} J for the best fit solution. Other estimates of E_r for the earthquake are the following: (1) 1.2×10^{14} J from local and regional seismograms and 0.69×10^{14} J from teleseismic P waves by X. Pérez-Campos (personal communication, 2013) and (2) 0.43×10^{14} J from teleseismic P waves by the National Earthquake Information Center (NEIC), U.S. Geological Survey. Although the ratio between our best fit model estimate and that from local and regional data is about 2.5, there is roughly an order of magnitude difference in the whole set of values, with E_r from dynamic inversion being at the high end. Such differences between regional and teleseismic estimates are common in the literature [*Singh and Ordaz*, 1994; *Pérez-Campos et al*., 2003]. We recall that our dynamic source parameters have been retrieved by fitting band-pass filtered (0.02 Hz–0.25 Hz) seismograms. The corner frequency, f_c, of the earthquake, estimated from S wave spectra, is ~0.47 Hz [*Singh et al*., 2013]. For an ω^2 Brune source model, which assumes an infinite rupture speed, the radiated energy contained in frequencies $f < f_c$ is less than 18% of the total [*Singh and Ordaz*, 1994]. This suggests that the dynamic source models developed to explain observations in the frequency band of 0.02 Hz–0.25 Hz retain some characteristics of the source at higher frequencies through a downscale causal relationship given by the elastodynamic and fault constitutive equations governing the propagating crack. This can be clearly seen in Figure S1 for a synthetic inversion, where the rupture speed of the target model (Figure S1, top right), which significantly varies in space, is almost perfectly retrieved by the best fit model solution at time scales shorter than 1 s (Figure S1, middle right) even though the "observed" seismograms were low-pass filtered in the same

Table 4. Inverted and Derived Source Parameters for the Zumpango Earthquake

	Parameter	Best Fit Model	Average Model
Inverted	$\Delta\tau$	27.7 MPa	29.2 ± 6.2 MPa
	$\Delta\tau_n$	58.5 MPa	60.0 ± 7.9 MPa
	D_c	0.71 m	0.74 ± 0.11 m
	$\Delta\mu$	0.036	0.03 ± 0.005
	A	78.4 km^2	88.5 ± 18.0 km^2
Derived	M_0	5.75×10^{18} Nm	$(9.54 \pm 2.27) \times 10^{18}$ Nm
	D_f	1.45 m	1.45 ± 0.21 m
	V_r/V_S	0.38	0.47 ± 0.09
	G	14.5×10^{14} J	$(14.4 \pm 3.5) \times 10^{14}$ J
	E_r	3.1×10^{14} J	$(5.4 \pm 3.1) \times 10^{14}$ J
	η_r	0.18	0.26 ± 0.10
	K	0.84	1.01 ± 0.22

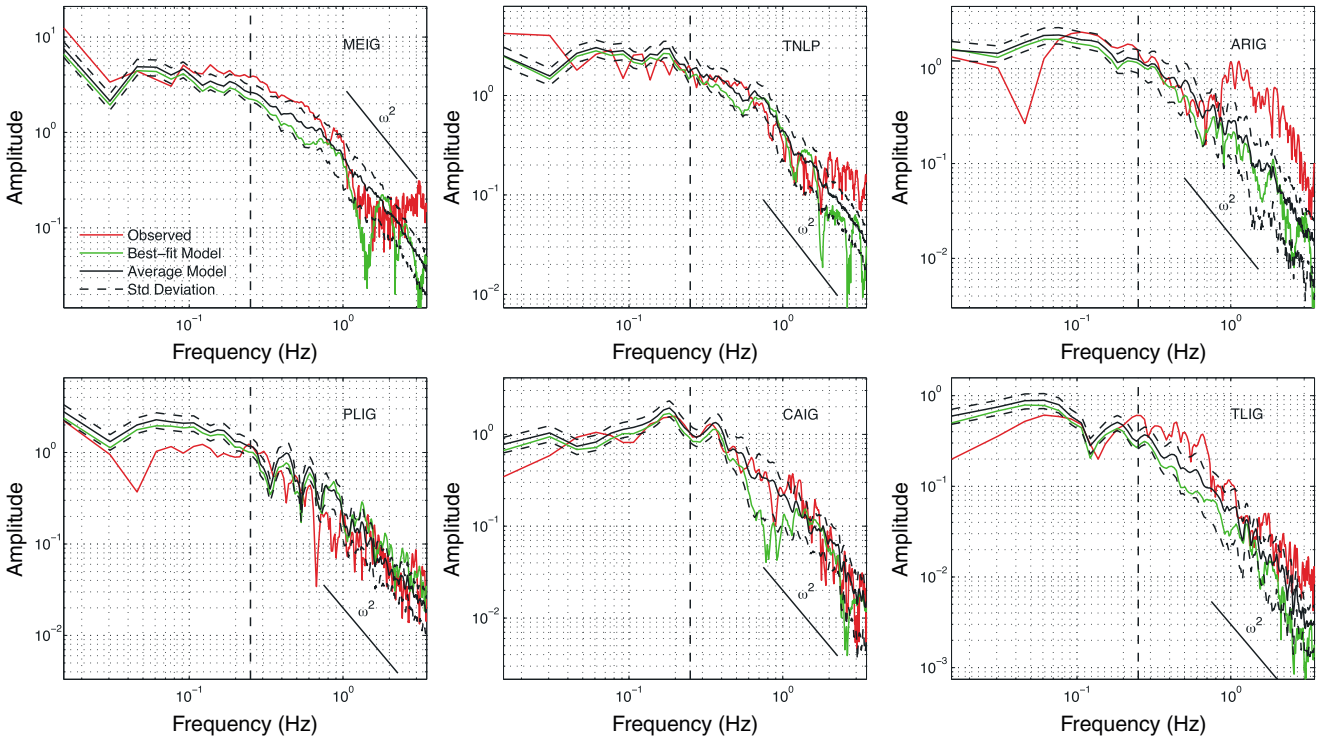

Figure 8. Displacement spectra of the Zumpango earthquake in the six stations used for dynamic inversion. The average (solid black) and the associated standard deviation band (dashed) correspond to the 300 solution models produced by the inversion. The upper cutoff frequency used for the inversion (0.25 Hz) is depicted with vertical dashed lines.

frequency band (i.e., $f < 0.25$ Hz). In other words, there exists an interscale causality in rupture dynamics that makes the wavefield at long periods to depend strongly on the small-scale source properties. As a result, the inversion may solve rupture details with characteristic times shorter than 4 s (i.e., the data cutoff period).

Figure S7 shows the percentile deviations of both the average and the best fit models yielded by the inversion of the band-pass filtered seismograms between 0.02 Hz and 0.5 Hz with respect to the average values reported in Table 4, which were obtained from the same seismograms but filtered between 0.02 Hz and 0.25 Hz. In accordance with our synthetic inversions including model uncertainties, these results show that the average solution model is closer (i.e., 36% closer; see bottom line of Table 3) to the reference solution than the best fit model. Besides, final seismogram misfits of the median and best fit models are 59% and 71% larger than those obtained from seismograms below 0.25 Hz. Although the average solutions for both frequency bandwidths are essentially the same (i.e., 20% average discrepancy; see bottom line of Table 3), given its outstanding waveform fitting, we keep the source parameters of Table 4 as our preferred model for the Zumpango earthquake.

Figure 8 examines the spectra of the earthquake corresponding to the inverted dynamic models but using the attenuation relationship determined by *García et al.* [2004] for intermediate-depth (i.e., intraslab) earthquakes in central Mexico. It illustrates *S* wave spectra (harmonic mean of the horizontal components) of the best fit model at the six stations and the average and ±1 standard deviation spectra of the 300 solution models. These spectra are plotted up to $f = 3.5$ Hz; beyond this frequency, the numerical noise results in contamination. The figure also includes observed spectra. As expected, the spectra corresponding to the dynamic models are in good agreement with the observed ones at $f < 0.25$ Hz. Not surprisingly, they deviate in some cases from the observed ones at higher frequencies. However, it is reassuring that they are realistic in shape, confirming that the dynamic models retain fundamental features of the source at high frequencies supporting the correctness of the interscale casualty of our dynamic source models.

4. Discussion

Both average rupture velocity ($V_r/V_S = 0.47 \pm 0.09$, hence, $V_r \sim 2.2$ km/s) and radiation efficiency ($\eta_r = 0.26 \pm 0.1$) of the Zumpango earthquake are remarkably low. These values, which are in accordance with theoretical

expectations for a Mode II dynamic crack propagation [*Kanamori and Rivera*, 2006], are typical of slow, interplate tsunami earthquakes [e.g., *Kanamori and Kikuchi*, 1993; *Venkataraman and Kanamori*, 2004]. Tsunami earthquakes are characterized by large (M_s-M_w) disparity [*Kanamori and Kikuchi*, 1993] and anomalously low value of E_r and the ratio E_r/M_0 [*Newman and Okal*, 1998; *Ammon et al*., 2006]. The radiated energy of the Zumpango event ($E_r = (5.4 \pm 3.1) \times 10^{14}$ J) is close to those of other Mexican earthquakes of similar M_0 irrespective of their faulting mechanism and depth (Pérez-Campos, personal communication, 2013). The same is true with its ratio $E_r/M_0 = 5.7 \times 10^{-5}$ in a large range of seismic moments (even for the value of E_r obtained from teleseismic records by the NEIC which is 1 order of magnitude smaller; see last section and Figure 11 of *UNAM Seismology Group* [2013]). This observation is not surprising for normal-faulting earthquakes in the subducted Cocos plate, which systematically produce high peak ground accelerations [*García et al*., 2005; *Singh et al*., 2013]. It seems then to be a paradox that prevents conciliating two main observations: (1) a slow and inefficient rupture process and (2) a remarkably high radiation of short period waves.

Low radiation efficiency and high E_r imply very high fracture energy, G (equation (9)), which makes this earthquake highly energetic. The available potential energy for the dynamic process of faulting is $\Delta W_0 = (1.98 \pm 0.66) \times 10^{15}$ J (equations (7) and (9)), from which we deduce that 73% or more (i.e., 82% for the best fit model; see Table 4) was not radiated (i.e., it was dissipated as fracture energy) and must have been used to propagate the rupture. Most shallow crust and interplate earthquakes have radiation efficiencies larger than 0.5 [*Venkataraman and Kanamori*, 2004], which implies $G < E_r$. For the Zumpango event, $\eta_r = 0.26 \pm 0.1$ (and $\eta_r = 0.18$ for the best fit model) so $G = 2.7E_r$ (and $G = 4.7E_r$ for the best fit model). In a closer view, our estimate for the specific fracture energy, G_c, or breakdown work density ($W_b = G/A$) as defined by *Tinti et al*. [2005] is close to 1.7×10^7 J/m^2 (Table 4), which is about 10 times larger than expected for shallow crust earthquakes based on a regression analysis by these authors. In contrast, as compared to other estimates for this kind of earthquakes by *Abercrombie and Rice* [2005] and *Lancieri et al*. [2012] using a different approach based on spectral analysis for ω^2 source models, although dispersion is high and the comparison is not obvious, the estimate for the Zumpango earthquake is in general agreement. In our simple slip-weakening friction model, this large amount of nonradiated energy is spent in mechanical work done by fault tractions during the stress breakdown. However, the actual manner in which it is partitioned to produce plastic strain, off-fault fracturing, heat, or any other dissipative process, especially at intermediate depths, still is a matter of debate, although resent observations favor the thermal shear runaway (with possible partial melting) as the dominant physical mechanism [*Prieto et al*., 2013]. What is true is that energy dissipation controls rupture speed. The higher the dissipation, the lower is V_r despite the high energy radiation observed for this earthquake.

The large stress drop determined for the Zumpango earthquake ($\Delta\tau = 29.2 \pm 6.2$ MPa, Table 4), which is in accordance with independent estimates for intraslab quakes in central Mexico [*García et al*., 2004], the observed low rupture speed, and high-energy dissipation are thus logical and compatible. Considering a slip-weakening distance of 0.7 m (Table 4) and taking $\dot{\overline{D}} = 1.8$ m/s as the mean slip rate during the initial dislocation phase (Figure 7), the stress breakdown should have taken place in about 0.4 s, which is a reasonable value even for crustal earthquakes [*Mikumo et al*., 2003; *Cruz-Atienza et al*., 2009]. The peak slip rate (PSR) is approximately reached at the time when the stress drop is completed [*Mikumo et al*., 2003; *Cruz-Atienza et al*., 2009] so that by taking 3.5 m/s as the maximum PSR (Figure 7) the focal particles acceleration produced by the stress drop should be close to 1 g (i.e., ~8.8 m/s^2) during the initiation and arrest of the rupture process.

Our source model is essentially a penny shape crack with radial rupture speed. For *Sato and Hirasawa*'s [1973] source model, which satisfies the exact slip solution for a circular shear crack by *Eshelby* [1957], we have $\Delta\tau \approx (7\pi/24)(V_s/V_r)\left(\mu\dot{D}/2V_s\right)$. Taking $V_s/V_r = 2.1$ (Table 4), this model predicts $\Delta\tau \approx 28.1$ MPa, which is consistent with our results. This is simply telling us that, given a slow rupture propagation process, to achieve accelerations close to 1 g in a deep focal region where the shear modulus is high, the stress drop must be several times (i.e., about 4 times) higher than those of shallower interplate earthquakes [*García et al*., 2004]. This also explains strong high-frequency radiation (and therefore large E_r) from intermediate-depth intraslab events despite their slow and inefficient rupture process, as previously discussed and shown for the earthquake studied here.

Error analysis discussed in section 2.4 and the supporting information yields a set of solution models satisfying the same ground motion misfit criterion. Differences between these models (e.g., between the

average and the best fit models) may be significant. However, estimates of the nondimensional K parameter (equation (10)) (1.01 ± 0.22 and 0.84 for the best fit model, Table 4), which reveals the general dynamic character of earthquakes, is constrained to a small region predicting subshear ruptures and perfectly in agreement with the range determined by *Ruiz and Madariaga* [2011, Figure 4] for their best solution models of the M_w6.7 intraslab Michilla earthquake. Our synthetic inversion tests also revealed that the average solution model is closer to the actual solution than the best fit model if uncertainty is present in the source location (Figure S5). The average model error for an epicentral mislocation of 8 km to the south, which is a reasonable value given the number of local stations used to relocate the event, is ~30% smaller than that of the best fit solution (see Table 3). In contrast, both errors are similar and close to 15% (Figure S6) if the bulk properties surrounding the source are 5% lower than the actual ones (see Table 3). Besides, the uncertainty associated to each parameter includes, in most of cases, the corresponding target value.

5. Conclusions

We have developed an inversion method for imaging the earthquakes source dynamics from regional records of ground motions. The method is based in genetic algorithms and is able to simultaneously solve hundreds of computationally expensive forward problems via MPI, like the one required here for modeling the spontaneous rupture process. The source model follows an elliptical patch approach where rupture is governed by constant parameters determining the static stress drop and the cohesive forces evolution through a slip-weakening constitutive law. Our method allows estimation of errors in both inverted and derived source parameters. If a good knowledge of the source location and the velocity structure is available, then the rupture speed (V_r), the rupture area (A), and the stress drop ($\Delta\tau$), which are difficult to resolve in kinematic source inversions, are well constrained and may have errors of ~30%, ~12%, and ~10%, respectively. In contrast, parameters like the radiated energy (E_r), the radiation efficiency (η_r), and the fracture energy (G) have larger errors, around ~70%, ~40%, and ~25%, respectively.

We applied the method to the M_w 6.5 intermediate depth (62 km) Zumpango earthquake and found two main features of the source process: (1) rupture speed ($V_r/V_S = 0.47 \pm 0.09$, i.e., about 2.2 km/s) and radiation efficiency ($\eta_r = 0.26 \pm 0.1$) were remarkably low and (2) energy radiation ($E_r = (0.54 \pm 0.31) \times 10^{15}$J and the ratio $E_r/M_0 = 5.7 \times 10^{-5}$) is similar to typical values for Mexican thrust events. These observations imply both large energy dissipation (i.e., more than 73% of ΔW_0, the available potential energy for the dynamic process of faulting) and large stress drop ($\Delta\tau = 29.2 \pm 6.2$ MPa) in the focal region. It is interesting to note that Zumpango earthquake and the deep 1994 Bolivian earthquake (M_w8.3; depth = 637 km) [*Kanamori et al*., 1998] share some fundamental features (i.e., slow rupture speed, low radiation efficiency, high stress drop, and small rupture area), as it also does the intermediate-depth seismicity of the Bucaramanga nest for the stress drop and the radiation efficiency [*Prieto et al*., 2013].

Acknowledgments

We thank Hiroo Kanamori, Steven Day, Jean Virieux, Sergio Ruiz, and Víctor Hugo Espíndola for fruitful discussions. The data for this paper are available upon proper request at the Servicio Sismológico Nacional (SSN) and the Instituto de Ingeniería, both at UNAM. This work was possible, thanks to the UNAM-PAPIIT grants IN119409, IN113814, and IN111314, the Mexican "Consejo Nacional de Ciencia y Tecnología" (CONACyT) under grant 80205, and the French "Agence Nationale de la Recherche" under grant ANR-2011-BS56-017.

References

Ammon, C. J., H. Kanamori, T. Lay, and A. A. Velasco (2006), The 17 July 2006 Java tsunami earthquake (Mw7.8), *Geophys. Res. Lett.*, *33*, L24308, doi:10.1029/2006GLO26303.

Andrews, D. J. (1976), Rupture velocity of plane strain shear cracks, *J. Geophys. Res.*, *81*, 5679–5687, doi:10.1029/JB081i032p05679.

Abercrombie, R. E., and J. R. Rice (2005), Can observations of earthquake scaling constrain slip weakening?, *Geophys. J. Int.*, *162*(2), 406–424, doi:10.1111/j.1365-246X.2005.02579.x.

Bizzarri, A., and M. Cocco (2003), Slip-weakening behavior during the propagation of dynamic ruptures obeying rate- and state dependent friction laws, *J. Geophys. Res.*, *108*(B8), 2373, doi:10.1029/2002JB002198.

Bouchon, M. (1981), A simple method to calculate Green's Functions for elastic layered media, *Bull. Seismol. Soc. Am.*, *71*, 959–971.

Brocher, T. M. (2008), Key elements of regional seismic velocity models for long period ground motion simulations, *J. Seismol.*, *12*, 217–221, doi:10.1007/s10950-007-9061-3.

Burridge, R., G. Kohn, and L. B. Freund (1979), The stability of rapid mode II shear crack with finite cohesive friction, *J. Geophys. Res.*, *85*, 2210–2222, doi:10.1029/JB084iB05p02210.

Campillo, M., S. K. Singh, N. Shapiro, J. Pacheco, and R. B. Herrmann (1996), Crustal structure south of the Mexican volcanic belt, based on group velocity dispersion, *Geofis. Int.*, *35*, 361–370.

Corish, S. C., R. Bradley, and K. B. Olsen (2007), Assessment of a nonlinear dynamic rupture inversion technique, *Bull. Seismol. Soc. Am.*, *97*(3), 901–914, doi:10.1785/0120060066.

Coutant, O. (1989), Program of numerical simulation AXITRA [in French], *Res. Rep. LGIT*, Univ. Joseph Fourier, Grenoble, France.

Cruz-Atienza, V. M., and J. Virieux (2004), Dynamic rupture simulation of non-planar faults with a finite-difference approach, *Geophys. J. Int.*, *158*, 939–954.

Cruz-Atienza V. M., and K. B. Olsen (2010), Supershear mach-waves expose the fault breakdown slip, in *Earthquake With Supershear Rupture Speeds*, edited by S. Das and M. Bouchon, *Tectonophysics*, *493*, 285–296, doi:10.1016/j.tecto.2010.05.012.

Cruz-Atienza, V. M., J. Virieux, and H. Aochi (2007), 3D finite-difference dynamic-rupture modelling along non-planar faults, *Geophysics*, *72*, SM123, doi:10.1190/1.2766756.

Cruz-Atienza, V. M., K. B. Olsen, and L. A. Dalguer (2009), Estimation of the breakdown slip from strong-motion seismograms: Insights from numerical experiments, *Bull. Seismol. Soc. Am.*, *99*, 3454–3469, doi:10.1785/0120080330.

Cruz-Atienza, V. M., A. Iglesias, J. F. Pacheco, N. M. Shapiro, and S. K. Singh (2010), Crustal structure below the Valley of Mexico estimated from receiver functions, *Bull. Seismol. Soc. Am.*, *100*, 3304–3311, doi:10.1785/0120100051.

Dalguer, L. A., and S. Day (2007), Staggered-grid split-node method for spontaneous rupture simulation, *J. Geophys. Res.*, *112*, B02302, doi:10.1029/2006JB004467.

Das, S., and K. Aki (1977), Fault plane with barriers: A versatile earthquake model, *J. Geophys. Res.*, *82*, 5658–5670, doi:10.1029/JB082i036p05658.

Das, S., and B. K. Kostrov (1990), Inversion for seismic slip rate history and distribution with stabilizing constraints: Application to the 1986 Andreanof Islands Earthquake, *J. Geophys. Res.*, *95*(B5), 6899–6913, doi:10.1029/JB095iB05p06899.

Day, S. M. (1982), Three-dimensional simulation of spontaneous rupture: The effect of nonuniform prestress, *Bull. Seismol. Soc. Am.*, *72*, 1881–1902.

Díaz-Mojica, J. (2012), Inversión de la dinámica de sismos mexicanos, McS thesis, Posgrado en Ciencias de la Tierra, Universidad Nacional Autónoma de México, Mexico City, Mexico.

Di Carli, S., C. Francois-Holden, S. Peyrat, and R. Madariaga (2010), Dynamic inversion of the 2000 Tottori earthquake based on elliptical subfault approximations, *J. Geophys. Res.*, *115*, B12328, doi:10.1029/2009JB006358.

Eshelby, J. D. (1957), The determination of the elastic field of an ellipsoidal inclusion and related problems, *Proc. R. Soc. London, Ser. A*, *241*, 376–396.

Fernández de Vega, F., and E. Cantú-Paz (2010), *Parallel and Distributed Computational Intelligence*, Studies in Comput. Intell., vol. 269, Springer, Berlin, doi:10.1007/978-3-642-10675-0.

Freund, L. B. (1989), *Dynamic Fracture Mechanics*, Cambridge Univ. Press, Cambridge, U. K.

García, D., S. K. Singh, M. Herraíz, J. F. Pacheco, and M. Ordaz (2004), Inslab earthquakes of central Mexico: Q, source spectra and stress drop, *Bull. Seismol. Soc. Am.*, *94*, 789–802.

García, D., S. K. Singh, M. Herráiz, M. Ordaz, and J. F. Pacheco (2005), Inslab earthquakes of central Mexico: Peak ground-motion parameters and response spectra, *Bull. Seismol. Soc. Am.*, *95*, 2272–2282.

Goldberg, D. E. (1989), *Genetic Algorithms in Search, Optimization and Machine Learning*, pp. 432, Addison Wesley, Reading, Mass.

Guatteri, M., and P. Spudich (2000), What can strong motion data tell us about slip weakening fault friction laws?, *Bull. Seismol. Soc. Am.*, *90*, 98–116.

Holland, J. H. (1975), *Adaptation in Natural and Artificial Systems*, pp. 228, Univ. Mich. Press, Ann Arbor.

Husseini, M. I. (1977), Energy balance for motion along a fault, *Geophys. J. R. Astron. Soc.*, *49*, 699–714.

Ida, Y. (1972), Cohesive force across tip of a longitudinal-shear crack Griffith specific surface energy, *J. Geophys. Res.*, *77*, 3796–3805, doi:10.1029/JB077i020p03796.

Ide, S., and M. Takeo (1997), Determination of constitutive relations of fault slip based on seismic wave analysis, *J. Geophys. Res.*, *102*, 27,379–27,391, doi:10.1029/97JB02675.

Iglesias, A., V. M. Cruz-Atienza, N. M. Shapiro, S. K. Singh, and J. F. Pacheco (2001), Crustal structure of south-central Mexico estimated from the inversion of surface waves dispersion curves using genetic and simulated annealing algorithms, *Geofis. Int.*, *40*, 181–190.

Kanamori, H., and E. E. Brodsky (2004), The physics of earthquakes, *Rep. Prog. Phys.*, *67*, 1429–1496.

Kanamori, H., and L. Rivera (2006), Energy partitioning during an earthquake, in *Earthquakes: Radiated Energy and the Physics of Faulting*, *Geophys. Monogr. Ser.*, vol. 170, edited by R. Abercrombie et al., pp. 3–13, AGU, Washington, D. C., doi:10.1029/170GM03.

Kanamori, H., J. Mori, E. Hauksson, T. H. Heaton, L. K. Hutton, and L. M. Jones (1993), Determination of earthquake energy release and ML using terrascope, *Bull. Seismol. Soc. Am.*, *83*, 330–346.

Kanamori, H., D. L. Anderson, and T. H. Heaton (1998), Frictional melting during the rupture of the 1994 Bolivian earthquake, *Science*, *279*, 839–842.

Kim, Y., R. W. Clayton, and J. M. Jackson (2010), Geometry and seismic properties of the subducting Cocos plate in central Mexico, *J. Geophys. Res.*, *115*, B06310, doi:10.1029/2009JB006942.

Kostrov, B. V. (1966), Unsteady propagation of longitudinal cracks, *J. Appl. Math. Mech.*, *30*, 1241–1248.

Kostrov, B. V., (1974), Seismic moment and energy of earthquakes, and seismic flow of rock [Engl. transl.], *Izv. Earth Phys.*, *1*, 23–40.

Lancieri, M., R. Madariaga, and F. Bonilla (2012), Spectral scaling of the aftershocks of the Tocopilla 2007 earthquake in northern Chile, *Geophys. J. Int.*, doi:10.1111/j.1365-246X.2011.05327.x.

Lemoine, A., R. Madariaga, and J. Campos (2002), Slab-pull and slab-push earthquakes in the Mexican, Chilean and Peruvian subduction zones, *Phys. Earth Planet. Inter.*, *132*(1–3), 157–175.

Madariaga, R. (1976), Dynamics of an expanding circular fault, *Bull. Seismol. Soc. Am.*, *66*, 639–666.

Madariaga, R., and K. B. Olsen (2000), Criticality of rupture dynamics in 3-D, *Pure Appl. Geophys.*, *157*, 1981–2001.

Madariaga, R., K. B. Olsen, and R. J. Archuleta (1998), Modeling dynamic rupture in a 3D earthquake fault model, *Bull. Seismol. Soc. Am.*, *88*, 1182–1197.

Marcinkovich, C., and K. Olsen (2003), On the implementation of perfectly matched layers in a three-dimensional fourth-order velocity-stress finite difference scheme, *J. Geophys. Res.*, *108*(B5), 2276, doi:10.1029/2002JB002235.

Menke, W. (2012), *Geophysical Data Analysis: Discrete Inverse Theory*, 3rd ed. (textbook), 293 pp., Academic Press (Elsevier), Oxford, U. K., doi:10.1016/B978-0-12-397160-9.00001-1.

Mikumo, T., and T. Miyatake (1978), Dynamical rupture process on a three-dimensional fault with non-uniform frictions and near field seismic waves, *Geophys. J. R. Astron. Soc.*, *54*, 417–438.

Mikumo, T., and T. Miyatake (1993), Dynamic rupture processes on a dipping fault, and estimate of stress drop and strength excess from the results of waveform inversion, *Geophys. J. Int.*, *112*, 481–496.

Mikumo, T., K. B. Olsen, E. Fukuyama, and Y. Yagi (2003), Stress-breakdown time and slip-weakening distance inferred from slip-velocity functions on earthquake faults, *Bull. Seismol. Soc. Am.*, *93*(1), 264–282.

Newman, A. V., and E. A. Okal (1998), Teleseismic estimates of radiated seismic energy: The E/M0 discriminant for tsunami earthquakes, *J. Geophys. Res.*, *103*(26), 885–898.

Olsen, K. B., et al. (2009), ShakeOut-D: Ground motion estimates using an ensemble of large earthquakes on the southern San Andreas Fault with spontaneous rupture propagation, *Geophys. Res. Lett.*, *36*, L04303, doi:10.1029/2008GL036832.

Pacheco, J. F., and S. K. Singh (2010), Seismicity and state of stress in Guerrero segment of the Mexican subduction zone, *J. Geophys. Res.*, *115*, B01303, doi:10.1029/2009JB006453.

Palmer, A., and J. R. Rice (1973), The grow of slip surfaces in the progressive failure of overconsolidated clay, *Proc. R. Soc. London, Ser. A*, *332*, 527–548.

Pérez-Campos, X., Y. Kim, A. Husker, P. M. Davis, R. W. Clayton, A. Iglesias, J. F. Pacheco, S. K. Singh, V. C. Manea, and M. Gurnis (2008), Horizontal subduction and truncation of the Cocos Plate beneath central Mexico, *Geophys. Res. Lett.*, *35*, L18303, doi:10.1029/2008GL035127.

Pérez-Campos, X., S. K. Singh, and G. C. Beroza (2003), Reconciling teleseismic and regional estimates of seismic energy, *Bull. Seismol. Soc. Am.*, *93*(5), 2123–2130.

Peyrat, S., and K. B. Olsen (2004), Nonlinear dynamic rupture inversion of the 2000 Western Tottori, Japan, earthquake, *Geophys. Res. Lett.*, *31*, L05604, doi:10.1029/2003GL019058.

Peyrat, S., and P. Favreau (2010), Kinematic and spontaneous rupture models of the 2005 Tarapacá intermediate depth, *Geophys. J. Int.*, *181*, 369–381.

Pikaia (2002), Sofware developed by P. Charbonneau and B. Knapp. [Available at www.whitedwarf.org/parallel.]

Prieto, G. A., M. Florez, S. A. Barrett, and G. C. Beroza (2013), Seismic evidence for thermal runaway during intermediate-depth earthquake rupture, *Geophys. Res. Lett.*, *40*, 1–5, doi:10.1002/2013GL058109.

Rivera, L., and H. Kanamori (2005), Representations of the radiated energy in earthquakes, *Geophys. J. Int.*, *162*(1), 148–155, doi:10.1111/j.1365-246X.2005.02648.x.

Ruiz, S., and R. Madariaga (2011), Determination of the friction law parameters of the Mw 6.7 Michilla earthquake in northern Chile by dynamic inversion, *Geophys. Res. Lett.*, *38*, L09317, doi:10.1029/2011GL047147.

Ruiz, S., and R. Madariaga (2013), Kinematic and dynamic inversion of the 2008 Northern Iwate earthquake, *Bull. Seismol. Soc. Am.*, *103*, 694–708.

Sato, T., and T. Hirasawa (1973), Body wave spectra from propagating shear waves, *J. Phys. Earth*, *21*, 415–431.

Singh, S. K., and M. Pardo (1993), Geometry of the Benioff Zone and state of stress in the overriding plate in Central Mexico, *Geophys. Res. Lett.*, *20*, 1483–1486, doi:10.1029/93GL01310.

Singh, S. K., and M. Ordaz (1994), Seismic energy release in Mexican subduction zone earthquakes, *Bull. Seismol. Soc. Am.*, *84*, 1533–1550.

Singh, S. K., J. F. Pacheco, B. K. Bansal, X. Pérez-Campos, R. S. Dattatrayam, and G. Suresh (2004), A source study of the Bhuj, India, earthquake of 26 January 2001 (Mw 7.6), *Bull. Seismol. Soc. Am.*, *94*(4), 1195–1206.

Singh, S. K., M. Ordaz, X. Pérez-Campos, and A. Iglesias (2013), Intraslab versus interplate earthquakes as recorded in Mexico City: Implications for seismic hazard, *Earthquake Spectra*, doi:10.1193/110612EQS324M.

Song, T.-R. A., D. V. Helmberger, M. R. Brudzinski, R. W. Clayton, P. Davis, X. Pérez-Campos, and S. K. Singh (2009), Subducting slab ultra-slow velocity layer coincident with silent earthquake in southern Mexico, *Science*, *324*, 502–506, doi:10.1126/science.1167595.

Spudich, P., and M. Guatteri (2004), The effect of bandwidth limitations on the inference of earthquake slip-weakening distance from seismograms, *Bull. Seismol. Soc. Am.*, *94*, 2028–2036.

Spudich, P., and D. P. Miller (1990), Seismic site effects and the spatial interpolation of earthquake seismograms: Results using aftershocks of the 1986 North Palm Springs, California, earthquake, *Bull. Seismol. Soc. Am.*, *80*, 1504–1532.

Suárez, G., T. Monfret, G. Wittlinger, and C. David (1990), Geometry of subduction and depth of the seismogenic zone in the Guerrero gap, Mexico, *Nature*, *345*, 336–338.

Tago, J., V. M. Cruz-Atienza, J. Virieux, V. Etienne, and F. J. Sánchez-Sesma (2012), A 3D hp-adaptive discontinuous Galerkin method for modeling earthquake dynamics, *J. Geophys. Res.*, *117*, B09312, doi:10.1029/2012JB009313.

Tinti, E., P. Spudich, and M. Cocco (2005), Earthquake fracture energy inferred from kinematic rupture models on extended faults, *J. Geophys. Res.*, *110*, B12303, doi:10.1029/2005JB003644.

UNAM Seismology Group (2013), Ometepec-Pinotepa Nacional, Mexico Earthquake of 20 March 2012 (Mw7.5): A preliminary report, *Geofis. Int.*, *52*(2), 173–196.

Vallée, M., and M. Bouchon (2004), Imaging coseismic rupture in far field by slip patches, *Geophys. J. Int.*, *156*, 615–630.

Venkataraman, A., and H. Kanamori (2004), Observational constraints on the fracture energy of subduction zone earthquakes, *J. Geophys. Res.*, *109*, B05302, doi:10.1029/2003JB002549.

Virieux, J., and R. Madariaga (1982), Dynamic faulting studied by a finite difference method, *Bull. Seismol. Soc. Am.*, *72*, 345–369.

Auxiliary material for

Dynamic Source Inversion of the M6.5 Intermediate-Depth Zumpango Earthquake in Central Mexico: a Parallel Genetic Algorithm

John Díaz-Mojica[1,3], Víctor M. Cruz-Atienza[1*], Raúl Madariaga[2], Shri K. Singh[1], Josué Tago[3] and Arturo Iglesias[1]

(*Corresponding author email: cruz@geofisica.unam.mx)

[1]Instituto de Geofísica, Universidad Nacional Autónoma de México
[2]École Normale Supérieur de Paris, France
[3]Institut des Sciences de la Terre, Université Joseph Fourier, France

Journal of Geophysical Research – Solid Earth
September 2014

Dynamic-Source Synthetic Inversion Tests

In this supplement we present results of several synthetic inversion tests based on the same method used to model the Zumpango earthquake, which is described in the main text of this paper. We first present results for a test where the velocity structure and the source location are known. Then, we consider more realistic cases where these hypotheses are relaxed.

In order to test the capability of our Genetic Algorithm to image the earthquake dynamics, we carried out several synthetic inversions with the problem setup of the intraslab normal-faulting event analysed in this study, which is shown in Figure 3. The model space considered in the inversions is given in Table 2 and Figure 2 (black lines). Here we only show results from one representative test. Seismograms used as observed data in the synthetic inversion were computed within a layered medium (Table 1) for a 62.6 km depth source model with strike = 102°, dip = 51° and rake = -95° (i.e., the auxiliary fault plane of the Zumpango quake) and moment magnitude Mw = 6.7. The dynamic parameters of the source model are: the stress drop in the ellipse $\Delta\tau = \tau_0 - \tau_d = 31.64$ MPa, the stress drop in the nucleation patch $\Delta\tau^n = \tau_0^n - \tau_d =$ 45.2 MPa, the change of the friction coefficient $\Delta\mu = 0.022$ and the slip weakening distance $D_c = 1.31$ m. Other parameters, required to complete the model description, are given in Section 2.1. Regarding the geometry of the target source, Figure A1 (first row) shows the dimensions, orientation and position of the elliptical patch with respect to the nucleation zone. The figure also shows the final slip, peak slip rate, rupture velocity and rupture times over the fault plane produced by this model, while the associated 0.25 Hz low-pass filtered seismograms (i.e., the 'data' in the inverse problem) are plot in Figure A2 (red curves). We have selected this model because of two main reasons: (1) because it has a narrow rupture patch, and (2) because it exhibits large rupture-speed variability (i.e., multiple transitions from subshear to supershear regimes). These properties of the target model make the synthetic

inversion very suitable to assess resolvability of both, the rupture geometry and the spatial variability of rupture speed.

To invert this data, we considered a model population of 270 individuals for the Genetic Algorithm (GA) multiscale inversion and 50 generations per step. Thus, the whole inversion procedure explored 27,000 dynamic rupture models. The initial and final mutation percentages per step were 60% and 2%, respectively. Figure A3 shows the evolution of the misfit function M (Equation 1) as a function of the GA generations. Although the best-fit model solution (red diamonds) evolves through long step overs, the population median (circles) exhibits a monotonic evolution, especially during the first two thirds of both successive inversions. Reductions of 75% and 60% of the median are achieved in the coarse and fine inversions, respectively. Notice that the two-step procedure promotes high convergence rates in the first and coarser inversion, and the exploitation of the best models in the finer inversion thanks to the homogenization of the population (i.e., the collapse of the 25 to 75 percentiles (blue bars) over the population median).

Solutions obtained by the GA for the synthetic inversion are excellent. As discussed in Section 2.4 based on results shown in Figure 2, convergence to the target source model was essentially achieved for the best-fit (red circles) and the weighted average (blue circles) solution models. Seismograms corresponding to both models are shown in Figure A2. Despite the large model space explored in the inversion (see the parameters variation ranges in Table 2 and Figure 2) and the strong nonlinearity of the problem, the multiscale approach converges toward the actual problem solution. This is achieved even though the target model exhibits large rupture-speed variability, with supershear transients after nucleation and by the end of rupture, around 2 s contours. This is clear in Figure A1, where the rupture speed of the target model (top right panel), which significantly varies in space, is almost perfectly retrieved by the best-fit model solution at time scales shorter than 1 s (middle right panel). Since the synthetic inversion was done considering exactly the same frequency bandwidth as for the Zumpango earthquake (f < 0.25 Hz), these results show that a downscale

causal relationship (from large to small problem scales), given by the elastodynamic and constitutive equations involved in our model, allows solving rupture details with characteristic times shorter than 4 s (i.e., the data cutoff period).

The synthetic inversion test makes it possible to quantify the sensitivity of the inverse problem to the model parameters. In this case, the selection criterion was such that $S_R < 25\ \%$ (Equation 2), so 325 individuals were kept in the final set of solution models. As detailed in Section 2.4, Figure 2 synthetizes the inversion results and shows that, except for the stress drop inside the nucleation patch ($\Delta\tau_n$), the other eleven parameters of the best-fit source model differ by less than ~5% of the target value (red circles). This can also be seen in Figure A4, which presents approximations of the probability density functions (PDF) (i.e., for a given GA sampling rate) for some model parameters along with their weighted means, standard deviations (sigma) and target values. Aside from the slip weakening distance, D_c, which has a bimodal distribution and, to a lesser extent, the stress drop, the rest of parameters (even those not shown) are satisfactorily described by Gaussian density functions. This allows us to quantify the problem sensitivity and thus the formal parameters errors from sigma estimates. We notice that D_c and the stress drop are two parameters difficult to constraint from the inversion of ground motions because of their local effect in the rupture process. In any case, values reported in Figure A4 for the rest of parameters show, for instance, that the inverse problem is more sensitive to the rupture area than the radiation efficiency (i.e., compare percentages of sigma relatives to the mean values). In this sense, we may conclude that parameters like the average rupture speed (V_r) and the rupture area (A) are well constrained in our dynamic source inversion, with errors smaller than ~30% and ~12%, respectively. The stress drop ($\Delta\tau$) seems to be also well recovered with an error of ~10%, although the PDF sampling by the GA prevents us to be confident on this conclusion. A denser sampling might be required to draw final conclusions on this parameter. In contrast, derived parameters, such as the radiated energy (E_r), the radiation efficiency (η) and the fracture energy (G) have larger errors, around ~70%, ~40% and ~25%, respectively. These estimates do not consider errors due to hypocentral mislocations and/or

uncertainties in the velocity structure and, therefore, on the Green functions. Estimating the PDFs by semi-global methods such as our GA is a powerful means when inverting highly non-linear problems, making these methods very attractive although computationally demanding.

A1.1 Uncertainty in the Earthquake Location and the Velocity Structure

In order to assess the model errors due to uncertainties in the hypocentral location and the velocity structure, we have performed two more synthetic inversions. In the first test, we have assumed an 8 km epicentral mislocation to the south of the target source hypocentre, while the rest of the model attributes are the same as those given in the last section. To this purpose, we have inverted the seismograms produced by the target model (i.e., the observed data) by assuming the Green functions between the stations and the incorrect hypocentral location to solve the forward problem during the inversion procedure. As we proceed with real earthquakes (see Section 3.1 of the main manuscript), before the inversion, the P-waves of the observed data were aligned with the theoretical arrival times for the incorrect location. Results of the test are gathered in Figure A5, where we report percentile differences of the average and best-fit model parameters with respect to those of the target model. Although differences are larger than those obtained without model uncertainties (compare with Figure 2 of the main text) notice that, in contrast with such an ideal case, the error of the average model is ~30% smaller than the error of the best-fit model (see Table 3 of the main text).

In the second test, we assumed that the elastic properties in the source region are 5% lower that those used to generate the seismograms of the target model (i.e., $V_P = 7.73\ km/s$, $V_S = 4.47\ km/s$ and $\rho = 3.25\ gr/cm^3$). Unlike kinematic source descriptions, dynamic earthquake models are intrinsically controlled by the bulk properties, namely the shear wave speed, β, and the rigidity, μ. Variations in these parameters have profound effects in the spontaneous rupture propagation and thus the radiated wavefield. Results of this test are presented in Figure A6, where we see

that mean errors of both the average and best-fit model are less than half of those from the previous test and close to 15% (see Table 3 of the main text).

Figures

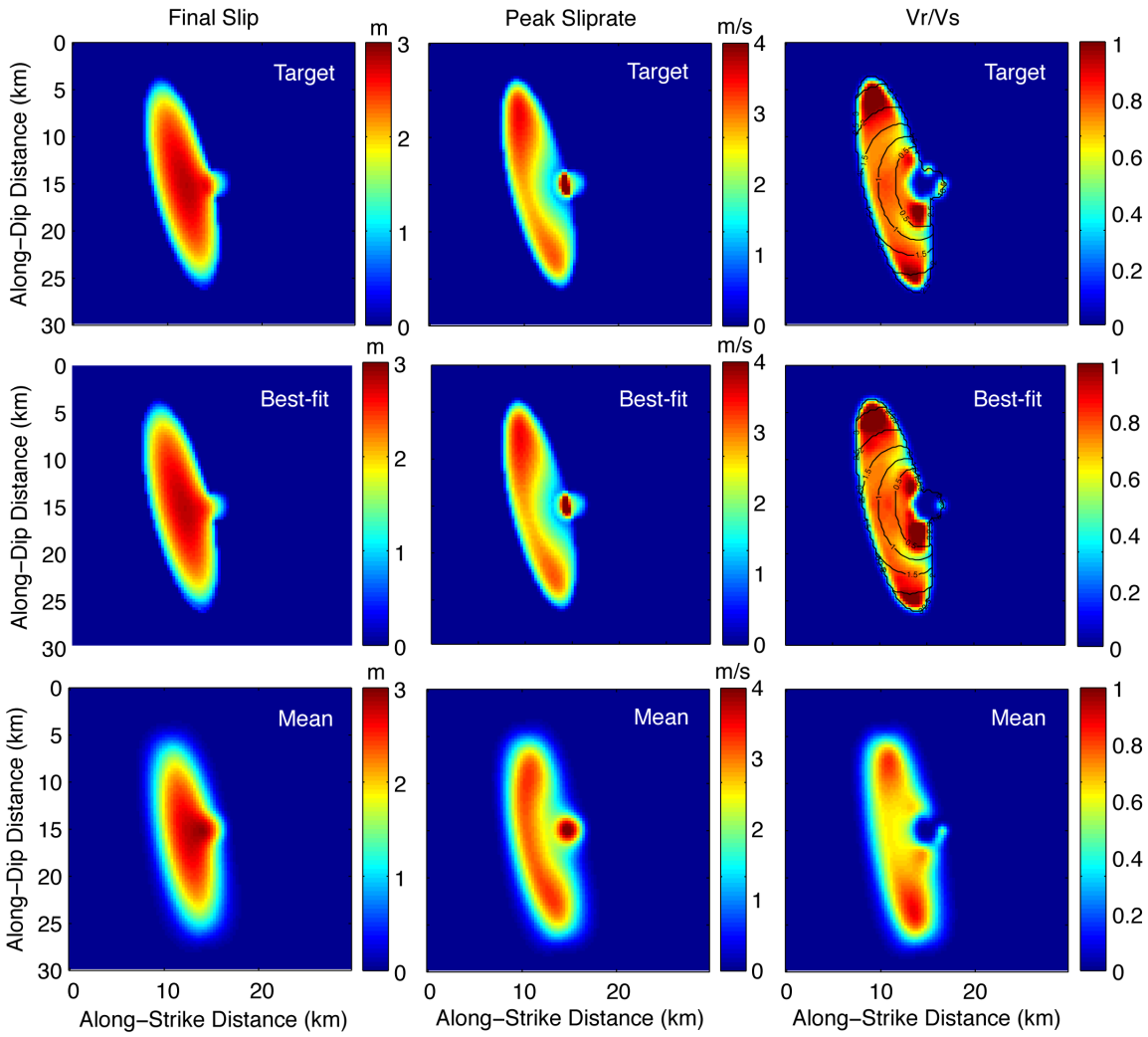

Figure A1 Target (top row), best-fit (middle row) and weighted average (Equation 4) (bottom row) source models over the fault plane for the synthetic inversion.

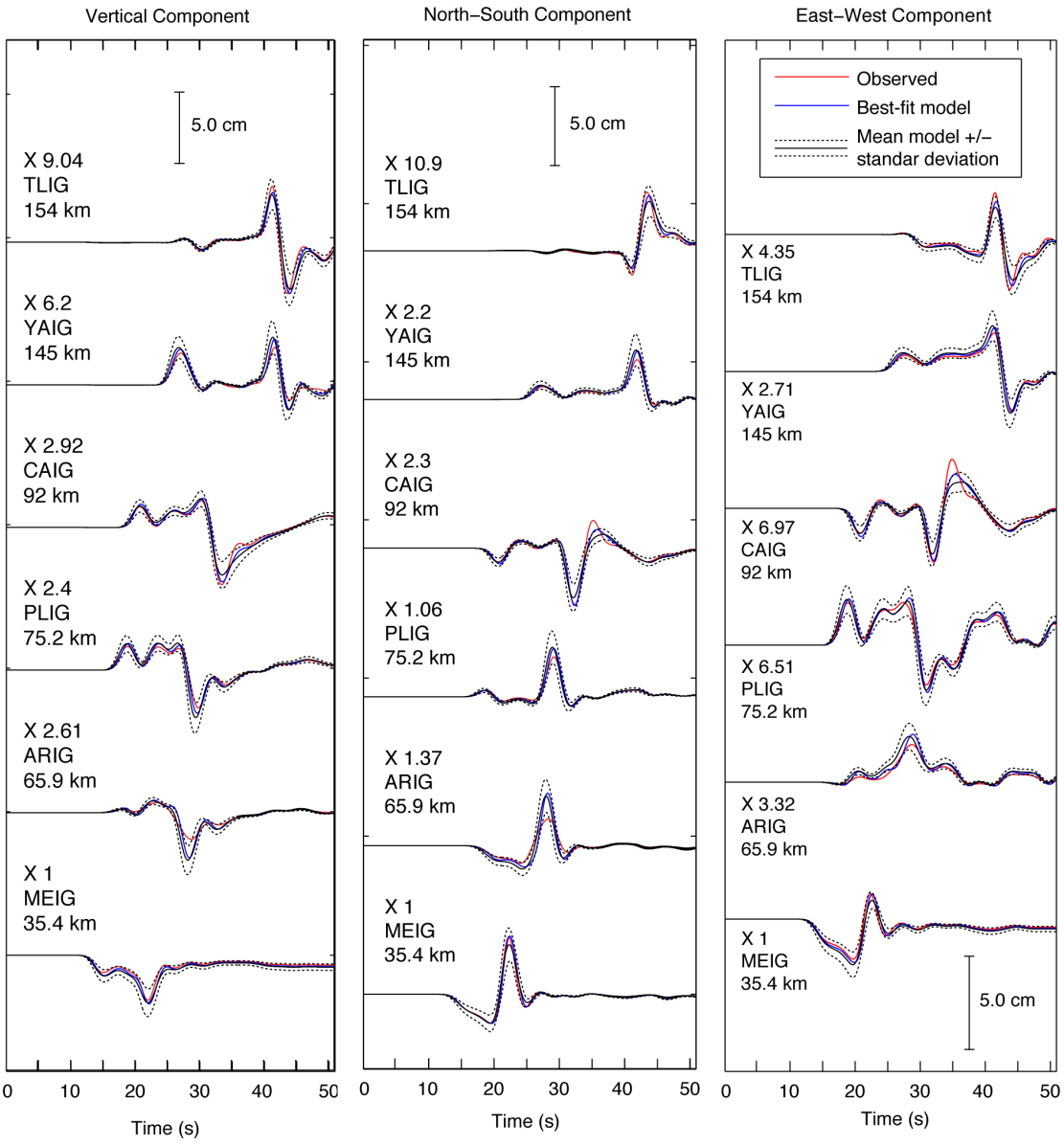

Figure A2 Seismograms fit yielded by the synthetic inversion. The stations distribution and the source mechanism are shown in Figure 3.

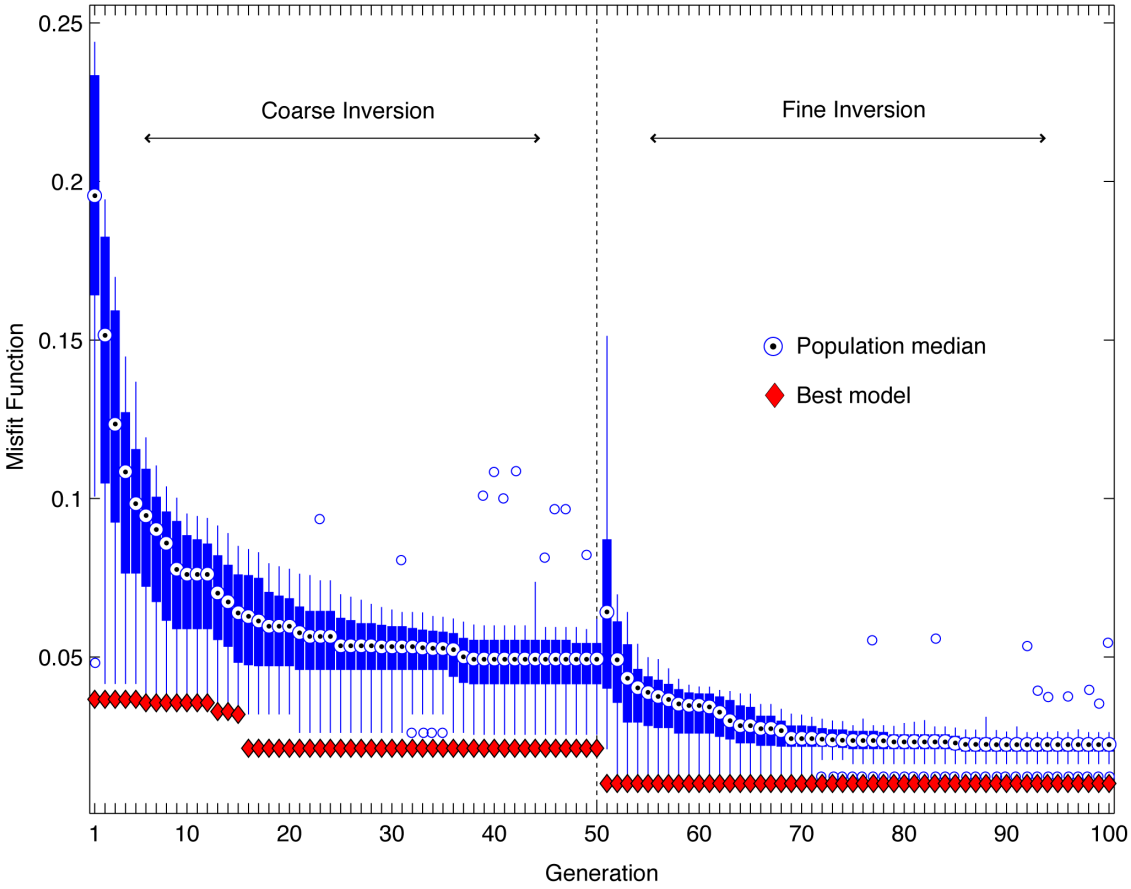

Figure A3 Misfit function (Equation 1) convergence during the two-step multiscale inversion procedure using the GA method.

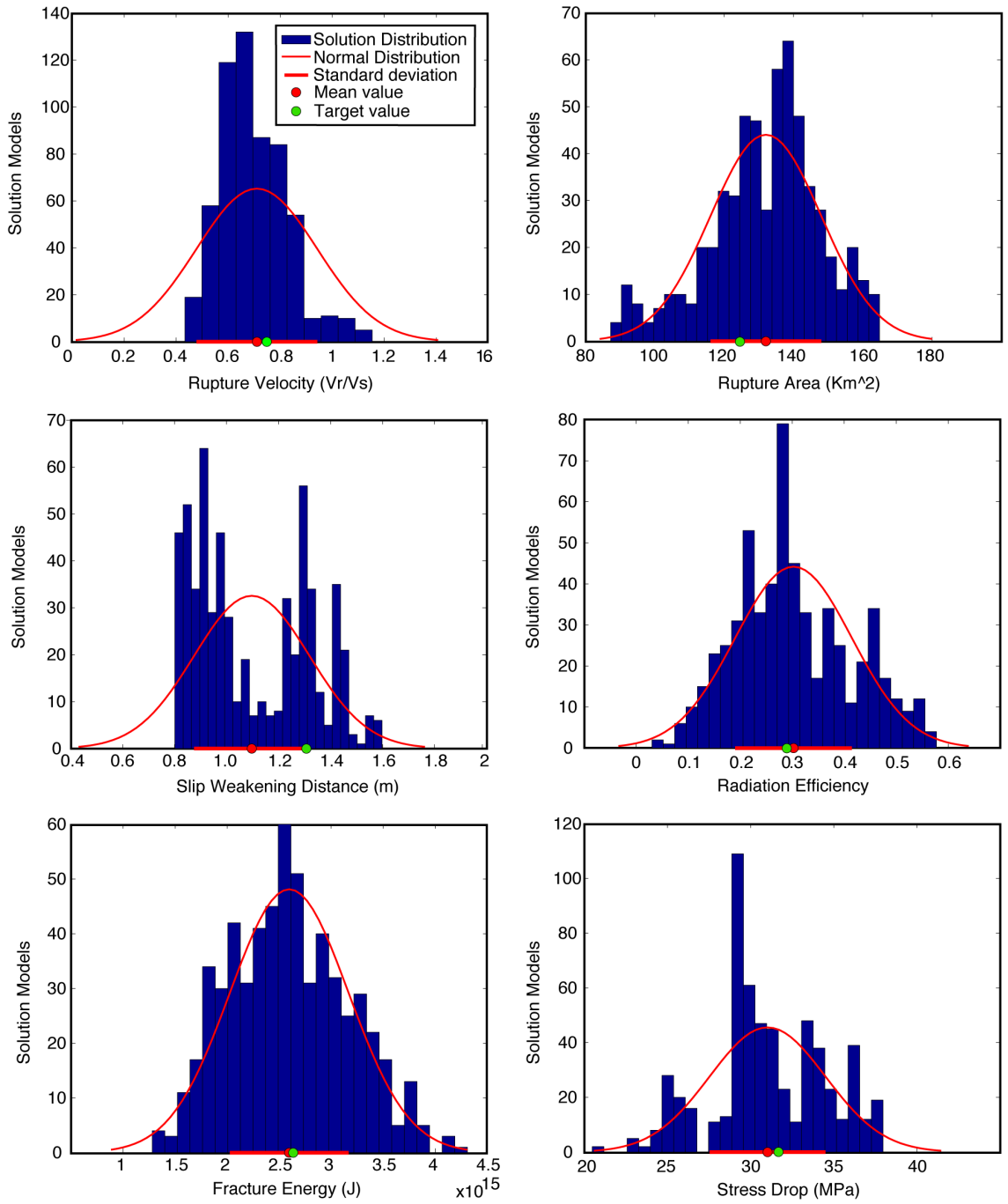

Figure A4 Parameter distributions for the set of solution models (blue bars), weighted means (Equation 4) (red circles), standard deviations (red bars) and target values (green circles). Best-fit normal distributions are depicted by the red curves.

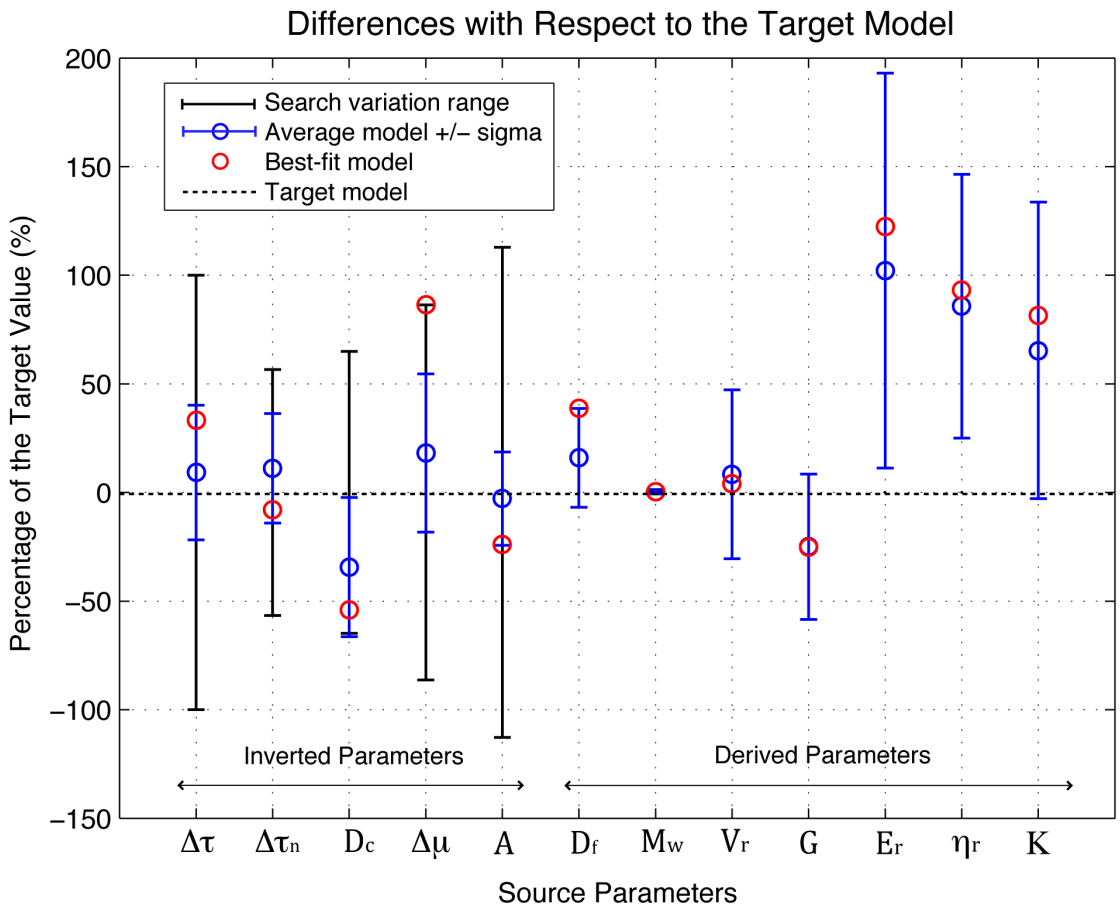

Figure A5 Convergence of the source parameters, error estimates and search variation ranges for the synthetic inversion with epicentral mislocation of 8 km to the south. The variation range for the rupture area, A, has been divided by 5 for plotting purposes.

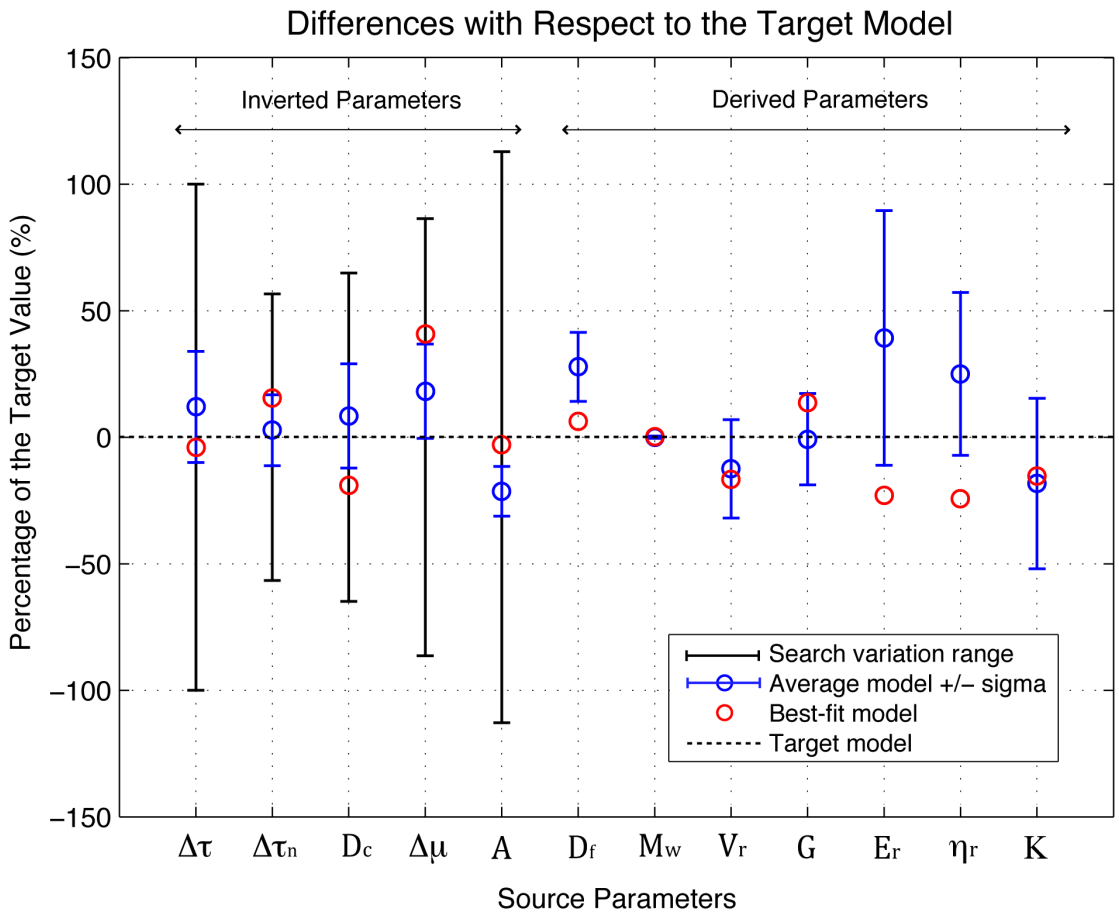

Figure A6 Convergence of the source parameters, error estimates and search variation ranges for the synthetic inversion with 5% reduction of the elastic properties in the source region. The variation range for the rupture area, A, has been divided by 5 for plotting purposes.

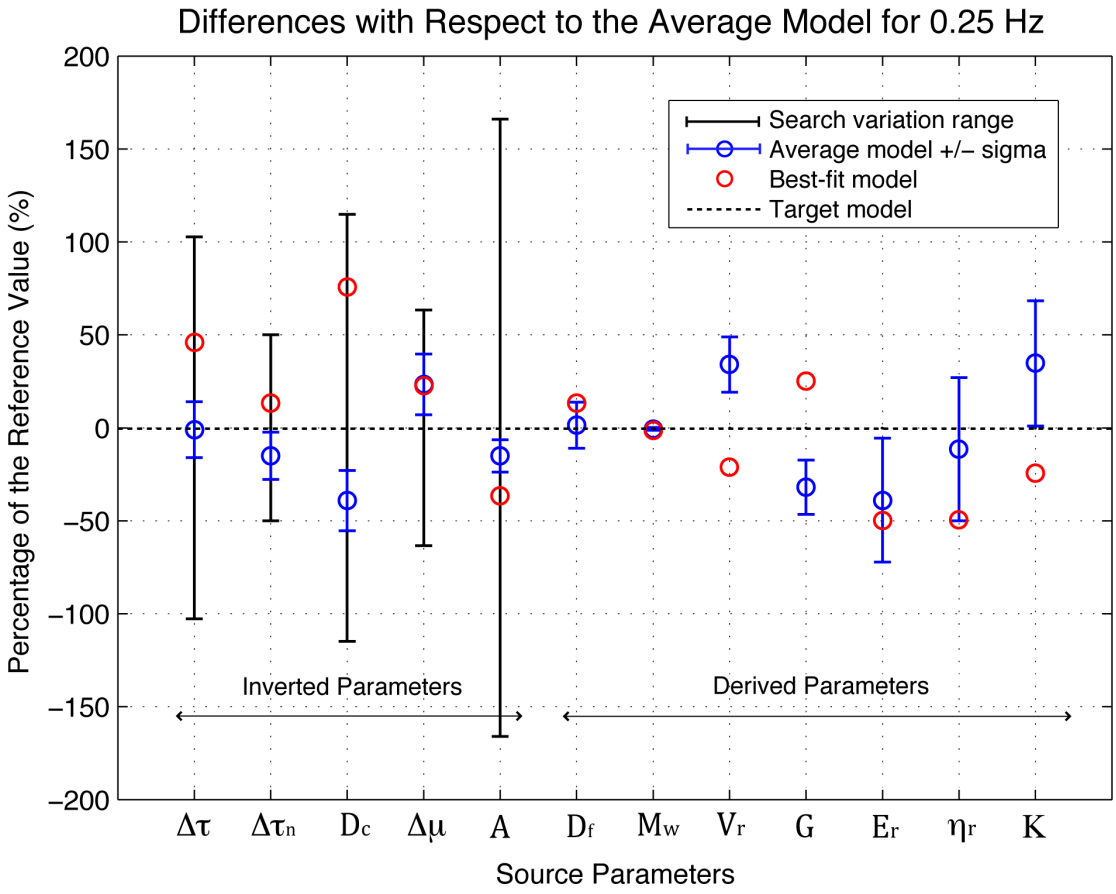

Figure A7 Convergence of the source parameters, error estimates and search variation ranges for the inversion of the Zumpango-earthquake real seismograms band-pass filtered between 0.02 Hz and 0.5 Hz. Errors are computed with respect to the average values reported in Table 4, which were obtained from the same seismograms but band-pass filtered between 0.02 Hz and 0.25 Hz. The variation range for the rupture area, A, has been divided by 5 for plotting purposes.